Journal of Materials Chemistry C

# Radiation Damage Effects in $Ga_2O_3$ Materials and Devices

| | |
|---|---|
| Journal: | *Journal of Materials Chemistry C* |
| Manuscript ID | TC-REV-08-2018-004193.R1 |
| Article Type: | Review Article |
| Date Submitted by the Author: | 06-Oct-2018 |
| Complete List of Authors: | Kim, Jihyun; Korea Univ.,<br>Pearton, Stephen; Univ.Florida, MSE<br>Fares, Chaker ; University of Florida, Department of Chemical Engineering<br>Yang, Jiancheng ; University of Florida, Department of Chemical Engineering<br>Ren, Fan; University of Florida, Department of Chemical Engineering<br>Kim, SuHyun; Korea Univ.<br>Polyakov, Alexander; National University of Science and Technology MISiS |
| | |

# Radiation Damage Effects in $Ga_2O_3$ Materials and Devices

Jihyun Kim[1,*], Stephen J. Pearton[2], Chaker Fares[3], Jiancheng Yang[3], Fan Ren[3], Suhyun Kim[1], and Alexander Y. Polyakov[4]

[1]Department of Chemical & Biological Engineering, Korea University, Anam-dong, Sungbuk-gu, Seoul, Korea

[2]Department of Materials Science and Engineering, University of Florida, Gainesville FL 32606 USA

[3]Department of Chemical Engineering, University of Florida, Gainesville FL 32606 USA

[4]National University of Science and Technology MISiS, Moscow, 119049, Leninsky Ave. 4, Russia

**Abstract**

The strong bonding in wide bandgap semiconductors gives them an intrinsic radiation hardness. Their suitability for space missions or military applications, where issues of radiation tolerance is critical, is widely known. Especially β-$Ga_2O_3$, an ultra-wide bandgap, is attracting interest for power electronics and solar-blind ultraviolet detection. Beside its superior thermal and chemical stabilities, the effects of radiation damage on $Ga_2O_3$ are of fundamental interest in space-based and some terrestrial applications. We review the effect on the materials properties and device characteristics of proton, electron, x-ray, gamma ray and neutron irradiation of β-$Ga_2O_3$ electronic and optoelectronic devices under conditions relevant to low earth orbit of satellites containing these types of devices.

* Corresponding author: Jihyun Kim (hyunhyun7@korea.ac.kr)

## Introduction

β-$Ga_2O_3$ is gaining attention because of its large bandgap of 4.8-4.9 eV and high estimated critical electric field ($E_C$) strength of ~8 MV/cm [1-21]. The large bandgap allows extending device operation to high temperatures, while the large critical field allows high voltage operation [1,2,4,6]. Figure 1(top) shows how this translates to potentially higher switching performance than other wide bandgap materials including GaN or SiC. Only diamond and AlN have higher figures-of-merit, but issues with cost and conductivity, respectively, limit their applicability [1,10]. The main electronics applications for β-$Ga_2O_3$ rectifiers and metal-oxide-semiconductor field effect transistors (MOSFETs) involve power conditioning and switching systems with low power loss during high frequency switching up to the GHz regime [6,9,10]. On the detector side, $Ga_2O_3$–based photodetectors are attracting interest as truly solar-blind deep ultraviolet (UV) photodetectors, since they exhibit cut-off wavelengths below 280 nm and have applications in military systems, air purification, space communication, ozone-layer monitoring and flame sensing [11,12]. Figure 1(bottom) shows the wavelength range covered by $Ga_2O_3$ and the related ternary alloys involving In or Al. The true solar-blindness of photodetectors based on β-$Ga_2O_3$ means they do not require any supplementary filter, in contrast to the case of GaAs or Si detectors [11,12].

A huge advantage for β-$Ga_2O_3$ in these applications is the availability of large diameter wafers. Bulk crystals have been grown by all the common techniques, including the Czochralski method (CZ), float-zone (FZ), edge-defined film fed (EFG) or Bridgman (horizontal or vertical, HB and VB) growth methods [2,7,19,20]. Wafers from these bulk crystals can obviously be used for devices like rectifiers, but also provide a template for growth of epitaxial films of controlled thickness and doping for active channel and contact layers [5,8,14,15,21] to allow achievement of

targeted device parameters such as breakdown voltage, on-state resistance and reverse recovery time.

The robustness of wide bandgap materials is especially advantageous in harsh environments caused by high temperature, pressure or radiation. Given the potential applications for $Ga_2O_3$ photoconductors and electronics, they could be subject to fluxes of high energy protons, alpha particles and electrons if used in low earth orbit satellites, as well as neutrons or gamma rays if used in radiation-hard nuclear or military systems [22-28]. Each of these forms of radiation produces different types of crystal lattice damage on the crystalline materials. In addition, primary defects may recombine, form complexes with each other, with dopants and with extended defects [29-33]. This may be more complicated in β-$Ga_2O_3$, which has two crystallographically inequivalent Ga positions, one with tetrahedral geometry, known as Ga(I) and one with octahedral geometry, known as Ga(II) [3,7,9,34]. Similarly, the oxygen atoms have three crystallographically different positions denoted as O(I), O(II) and O(III), respectively. Two oxygen atoms are coordinated trigonally and one is coordinated tetrahedrally. The lattice structure is shown schematically in Figure 2(a), while the two major crystal planes used for devices are shown in 2(b). This complexity means there are a larger number of possible defect complexes that could form upon irradiation.

At high incident energies, the energy of the primary recoils formed by collisions with lattice atoms becomes so high that they produce collision cascades and form heavily disordered regions (domains) with a very high defect density in the core [29-31,35,36]. The collision between an incoming ion and a lattice atom displaces the atom from its original lattice position, leading to vacancies, interstitials and complexes of both, and potentially with impurities in the $Ga_2O_3$ [37,38]. If an incident energetic particle such as a neutron or proton collides with the nucleus of a lattice

atom, the primary knock-on atom may be displaced from the lattice if the incident particle has sufficient energy ($E > E_d$), where $E_d$ is the lattice displacement energy [28-30].

**Importance of Radiation Damage in Electronics**

There are a number of fundamental materials parameters important in radiation damage studies, including the ionization energy and capture cross section of the hole or electron traps created and the carrier removal rate for each type of incident radiation, which will determine the lifetime of electronics in radiation environments. These are of interest because of the space radiation encountered by satellites [39], potential high altitude nuclear explosions and robotic inspection systems used near reactor cores or in accident response. The main concerns are the response of electronics to total ionizing dose displacement damage (crystal and interface damage) and single event effects (transients and bit flips due to single energetic particles) [22-29].

For space-based applications, it is of note that the Earth is surrounded by two regions (the Van Allen radiation belts) containing charged particles trapped in the Earth's magnetic field [39]. The inner belt, extending from 1,200-6,500 km (2.5 Earth radii) above the Earth's surface, is relatively stable whereas the outer belt, which extends from 13,000-40,000 km (10 Earth radii), is highly variable. The belts are separated by a gap, known as the slot region, containing few energetic electrons (Figure 3). The high-energy ionizing particles in this space environment are responsible for the anomalies observed in electronics and fall into three categories [22-27]:

(i) the Van Allen belts containing charged particles like electrons and protons. The inner belt comprises protons up to 600 MeV and electrons up to several MeV, while the outer belt has electrons and protons (0.1 to 5 MeV). The slot region between the belts may be enhanced for a

year following solar events. These events last several days and comprise both protons and heavier ions. Energies range up to several hundred MeV [39].

(ii) solar flares producing protons (up to 500 MeV) and a smaller component of heavy ions (up to 10 MeV/nucleon). The flare occurrence is influenced by the solar cycle [40].

(iii) cosmic rays, originating outside the Solar System, leading to a continuous background of ions whose energies can be very high. Earth's magnetosphere is bombarded by this nearly isotropic flux of energetic charged particles-85% protons, 14% α-particles, and 1% heavier ions covering the full range of elements. These are partly kept out by Earth's magnetic field. Primary cosmic rays interact with air nuclei to generate a cascade of secondary particles comprising protons, neutrons, mesons and nuclear fragments. Intensity of radiation a maximum at 18 km and drops off to sea level. At normal aircraft cruising altitudes the radiation is several hundred times the ground level intensity and at 18 km a factor three higher [41-44].

Neutron irradiation tends to create disordered regions in the semiconductors, while the damage from the other forms of radiation is more typically point defects. In all cases, the damaged region contains carrier traps that reduce the conductivity of the semiconductor and at high enough doses, a severe degradation of device performance [30-33,45,46]. The behavior of neutral radiation like gamma rays passing through semiconductors is fundamentally different than the interaction with charged particles such as protons, electrons or alpha particles and the energy loss mechanisms are the photoelectric effect, Compton scattering and pair production for γ- and x-rays while nuclear ("billiard-ball collisions") and electronic loss (ionization, heat) are the dominant mechanisms for ionizing radiation [29-36].

These particles produce various effects on semiconductor devices, including the accumulation of ionizing dose deposition over a long period, known as total ionizing dose (TID)

effect [40-44]. This mainly results from the most prevalent particles (electrons and protons) and leads to degradation of the electrical performance of devices. The accumulation of non-ionizing dose deposition due to protons or high energy electrons generates lattice defects leading to displacement damage effects (DD). These are critical in some classes of devices (sensors, charge-couple devices, amplifiers) and induce degradation of electrical parameters or increased background noise. Finally, there are the transient effects from a single particle in a sensitive region of the devices, called Single Event Upsets or Events (SEU or SEE) [29,39-45]. This instantaneous perturbation is due to protons and heavy ions and leads to functional anomalies in most kinds of devices [41-44].

For all of the ionizing particles within the atmosphere, the particle energy and flux varies with altitude and latitude [39]. The rate of SEU's observed in avionics correlates with the atmospheric neutron flux created by the interaction of cosmic rays with the oxygen and nitrogen atoms in the air at elevated altitudes [40,41]. The major concern in this case is random access memories (RAMs), both static and dynamic RAMs, because these contain the largest number of bits susceptible to upset [23-27]. The common method for dealing with SEU in RAM's is by error detection and correction (EDAC) [27]. Commercially available computer systems for aircraft incorporate EDAC in their designs. In addition to upset, other SEEs, such as latch-up and burnout, although less probable, also cause concern[23-26]. Charged particles in the atmosphere are also reaction products from the interaction of the primary cosmic rays with the O and N nuclei in the air. These include protons, pions, kaons, and electrons, with the pions and kaons decaying to muons. Most focus is on protons since they also cause SEEs [39,41-42]. The distribution of protons is similar to that of neutrons, with respect to energy and altitude [39]. The flux of the heavy ions

within the primary cosmic rays is rapidly attenuated with increasing atmospheric depth due to interactions with the atmosphere that fragment and thereby remove these heavy ions [39].

Most telecommunications satellites are located in geosynchronous orbit (Geo), located at the outer edge of the outer radiation belt [39]. Most navigation satellites, such as GPS and Galileo, operate in medium Earth orbit and pass through the heart of the outer radiation belt where they may subsequently experience much higher levels of radiation. Most Earth-observation satellites operate in low Earth orbit and may experience higher radiation levels if their orbits traverse the South Atlantic Anomaly or the auroral zones. The variability in flux of relativistic electron (E > 1 MeV) in the radiation belts is caused by changes in the solar wind by activity on the Sun.

The radiation damage suffered by microelectronics are [22-29]:

(i) Total Dose Effects-usually the factor that limits the operational lifetime of spacecraft electronics. As the dose accumulates, the changes in electrical properties of the semiconductor drive the component parameters outside of the design range for the circuits in which they are used and cause the circuit to cease proper functioning.

(ii) Displacement Damage, a cumulative effect resulting from prolonged exposure to the radiation environment. Displacement damage is caused by relatively low-energy atomic particles, as they transfer energy to the semiconductor lattice. These low-energy particles may be either directly present in the environment or produced indirectly by nuclear interactions in the device material or shielding. These particles displace atoms from their crystal lattice locations, creating defects in the crystal structure. These trap conduction electrons, increasing the resistance of the device.

(iii) Single Event Effects are changes in a microelectronic device caused by being hit by a single energetic particle [25,26]. SEE is electrical noise induced by the space

environment and results in data corruption, transient disturbance, high current conditions and result in non-destructive and destructive effects. Single Event Upsets cause a change of state in storage elements, while Single Event Functional Interrupts (SEFI) are events leading to temporal loss of device functionality and can be recovered by reset. Single Event Transients (SET) are transients on external signals leading to erroneous data. SEFI are caused by a single ion strike, similar to the usual single event upsets in memory devices. However, SEFI is manifested in a somewhat different manner. SEFI leads to a temporary non-functionality (interruption of normal operation) of the affected device. It may last as long as the power is maintained in some cases, while in others it may last for a finite period [25-26,40-44].

Table I shows a compilation of current and future requirements for total dose and single event upset radiation hardness of microelectronics [47].

**Radiation Damage in Wide Bandgap Semiconductors**

The strong bonding in wide bandgap semiconductors gives them an intrinsically high radiation resistance [1,9,18,31-36,44-46]. The fluence of ionizing radiation at which materials and devices such as transistors and light-emitting diodes made from SiC, GaN and related materials start to show degradation is about two orders of magnitude higher than in their GaAs equivalents [9,31-36,44-46]. This difference is at least partially attributed to the stronger bonding of these materials. A measure of this bond strength is the energy required to displace an atom from its lattice position or simply the atomic displacement energy. This parameter has been measured in several semiconductors and empirically determined to be inversely proportional to the volume of the unit cell [30-32]. This also generally scales with energy bandgap, so that these wide bandgap materials

have intrinsically higher radiation resistance than Si. From the known size of the $Ga_2O_3$ unit lattice [3,6,7], it should be quite radiation hard. β-$Ga_2O_3$ has lattice constants of $a$ = 12.2 Å, $b$ = 3.0 Å, and $c$ = 5.8 Å. As a rough estimate of expected bond strength we take the average lattice constant of the b and c distances, i.e. 4.4 Å, we would expect a similar radiation hardness to that of GaN [29-33].

The displacement energy threshold plays a crucial role in determining the induced defect concentration for incident electrons having energies <750 keV. The number of Frenkel pairs $N_d$ created by an incident particle can be approximated by $N_d = \kappa\hat{E}/2E_d$, where κ is the displacement efficiency and $\hat{E}$ is the energy given up in creating atomic displacements [29-33]. This is referred to as the non-ionizing energy loss or the nuclear stopping component. For higher energy or heavier particles, the approximation for $N_d$ is less accurate. However, it has been pointed out by Weaver et al.[33] that while fewer defects are created in GaN than in GaAs because of the larger values of $E_d$, the difference (36%) is insufficient to explain the order-of-magnitude (1000%) difference in radiation tolerance. They suggested that creation of Ga vacancies, which are triple acceptors, causes the number of acceptors to significantly increase and ($N_d - N_a$) to decrease [33]. It is not yet clear whether a similar explanation can be applied to other wide bandgap materials, or this is specific to the case of GaN. However, $V_{Ga}$ acceptors are among the dominant defects present in $Ga_2O_3$, even in the as-grown state [48-52].

How do the properties of $Ga_2O_3$ relate to radiation effects? The total ionizing doses that cause charge accumulation in field oxides in metal-oxide-semiconductor (MOS)–based devices results in the well-known shifts in threshold voltage, but if $Ga_2O_3$ transistors use Schottky metal gates, this is less of an issue [1,4]. There are also the SEU effects that result from the transit of energetic ions passing through the semiconductor, creating electron-hole pairs. The device

structures employed in wide bandgap semiconductors involving heterostructures tend to mitigate this effect. However, $Ga_2O_3$ rectifiers use thick active layers and will be more sensitive than a high-electron-mobility transistor (HEMT)-type device. Figure 4 shows the projected range of protons and alpha particles in $Ga_2O_3$ as a function of energy [28]. Note that the ranges extend well beyond the typical active layer thicknesses of $Ga_2O_3$ rectifiers or MOSFETs. The calculated vacancy distributions are shown in Figure 5, with an expanded view of the near-surface region. Note that these are maximum values, since defect recombination is significant in wide band gap semiconductors during irradiation [31,36,53]. The thickness issue also affects dose-rate radiation effects, which are sensitive to the total volume of a device. The last issue is lattice displacements that typically create traps and recombination sites in the device that degrade the carrier density through trapping and carrier mobility, with both of these mechanisms scaling with radiation dose. Si MOSFETs also suffer from single-event burnout when the charge from an energetic ion creates sustained conduction of the inherent parasitic bipolar transistor and single-event rupture when charge build-up near the gate causes a breakdown in the gate oxide. $Ga_2O_3$ MOSFETs are not yet at the level of sophistication where this is likely to be a controlling issue [9,10]. An additional factor is that wide bandgap devices generally employ higher critical fields and smaller active volumes that reduces radiation-induced charge collection.

Korhonen et al.[48] investigated the electrical compensation in n-type $Ga_2O_3$ by Ga vacancies using positron annihilation spectroscopy. They estimated a $V_{Ga}$ concentration of at least $5 \times 10^{18}$ $cm^{-3}$ in undoped and Si-doped samples. Since theoretical calculations predicts that these $V_{Ga}$ should be in a negative charge state for n-type samples [34], they will compensate the *n*-type doping [48]. Kananen et al.[49,50] used electron paramagnetic resonance (EPR) to demonstrate the presence of both doubly ionized ($V_{Ga}^{2-}$) and singly ionized ($V_{Ga}^{-}$) acceptors at room

temperature in CZ $Ga_2O_3$. They observed singly ionized gallium vacancies $V_{Ga}^-$ in neutron irradiated β-$Ga_2O_3$. The two holes in this acceptor are trapped at individual oxygen ions located on opposite sides of the gallium vacancy. A schematic of the $V_{Ga}$ derived from EPR is shown in Figure 6. For the sites of interstitial Ga and O, interstitial Ga and O locate at the same site. The O vacancy, Ga vacancy, Ga interstitial and O interstitial ($N_{Ga2O3}O_i$) are represented as 1, 2, and 3, respectively, in Figure 7 [54].

**Summary of Radiation Damage Studies in $Ga_2O_3$**

**(i) Neutron Damage Effects**

Cojocaru [37] reported the effect of fast neutrons on the electrical conductivity and thermoelectric power in β-$Ga_2O_3$. The conductivity was found to decrease while the thermoelectric power increased after an irradiation of $10^{17}$ $cm^{-2}$. This was explained by assuming that the defects introduced acted as electron traps. The defects annealed out at 1000 K with an activation energy of 2 eV and were assumed to be most likely $V_{Ga}$. Arehart et al. [55,56] irradiated n-$Ga_2O_3$ with 2 MeV neutrons to a fluence of $4 \times 10^{15}$ $cm^{-2}$. This produced a decrease in reverse current in rectifier structures, a loss of carriers at a rate of ~20 $cm^{-1}$ and the introduction of a deep trap state at $E_C$-1.88 eV observed in deep level transient spectroscopy (DLTS) measurements. This was tentatively ascribed to an oxygen-vacancy related state.

$Ga_2O_3$ was also investigated for detection for fast (14 MeV) neutrons[57], utilizing the $^{16}O(n,\alpha)^{13}C$ reaction. Diamond and 4H-SiC have previously been investigated as nuclear detectors under extreme conditions, involving temperatures up to 700 °C for 4H-SiC and 200 °C for diamond [57]. These temperature limits are limited by contacts and packaging rather than the intrinsic limits of the semiconductor. In the long term, it raises the need for simultaneous

research on the performance enhancement of the limiting factors. For $Ga_2O_3$-based detectors, Pt was used as a Schottky contact on conducting $Ga_2O_3$ wafers, with rear Ti/Au Ohmic contacts [57]. Insulating samples with Ti/Au Ohmic contacts on both sides were examined for comparison with the conducting samples. The insulating samples could be operated up to voltages of 1000 V [57]. The fast neutrons could be detected under these conditions, but with insufficient resolution for spectroscopy.

The displacement cross-section for $Ga_2O_3$ irradiated by neutrons was reported by Chaiken and Blue [58]. The results in Figure 8 show a monotonically increasing relation between incident neutron energy and displacement damage cross section. Slight variations in the monotonic trend are seen in the resonance regions of the interaction cross section. The curve is cutoff at low energy, because the analysis is cutoff at the neutron energy for which the maximum imparted energy, is less than the minimum displacement threshold energy in $Ga_2O_3$, $E_{\mathrm{Ga}}^{d}$ = 25 eV [58]. The displacement damage cross section was $\sigma_{\mathrm{Ga_2O_3}}^{\mathrm{disp}}$ (1 MeV) = 92.3 MeVmb. This is useful for comparing effects of neutron irradiation with differing fluences and energy spectra. The calculation of neutron displacement damage dose can be used to develop a damage effects correlation for other radiation particle types based on the displacement damage dose.

**(ii) Fast Ion Damage**

The anisotropic expansion and amorphization of $Ga_2O_3$ irradiated with 946 MeV Au ions was examined [38]. Damage saturation below amorphisation in ion implanted β-$Ga_2O_3$ using P, Ar and Sn ions with ion fluences from $10^{11}$-2 × $10^{15}$ $cm^{-2}$ has also been reported [53]. The concentration of displaced lattice atoms increased with ion fluence up to a saturation value of 90%. Further implantation only led to a broadening of the distribution, while the concentration remained at 90%. The ion fluence dependence of maximum damage concentration was modelled

assuming presence of point defects (which can recombine with those already existing from previous ion impacts) and non-recombinable damage clusters [53]. The damage dominantly consisted of randomly displaced lattice atoms, i.e. point defects and their complexes. For higher damage levels, there was also a contribution from correlated displaced lattice atoms, suggesting the damage clusters are not amorphous [53].

**(iii) Proton Damage in $Ga_2O_3$ Nanobelt Transistors**

Proton damage in back-gated field-effect transistors (FETs) fabricated on exfoliated β-$Ga_2O_3$ nano-layers (nanobelts) was studied for fluences of 10 MeV protons [18]. The radiation damaged FETs showed a decrease of 73% in the field-effect mobility and a positive shift of threshold voltage after proton irradiation at $2 \times 10^{15}$ $cm^{-2}$, which corresponds to approximately $10^5$ times the intensity of a solar proton event. The on/off ratio of the FETs was maintained even after proton doses of $2 \times 10^{15}$ $cm^{-2}$. The data are summarized in the drain-source characteristics of Figure 9, which show the effect of proton dose [18]. Doses of 1-2 $\times 10^{15}$ $cm^{-2}$ both lead to significant suppression of drain current. The radiation-induced damage in β-$Ga_2O_3$-based FETs was significantly recovered after annealing at 500 °C. This temperature is similar to that needed for removal of plasma-induced dry etch damage in $Ga_2O_3$ [59].

**(iv) Proton Damage in $Ga_2O_3$ Rectifiers**

10 MeV proton irradiation of vertical geometry $Ga_2O_3$ rectifiers at a fixed fluence of $10^{14}$ $cm^{-2}$ produced trap states that reduced the carrier concentration in the $Ga_2O_3$, with a carrier removal rate of 235.7 $cm^{-1}$ for protons of this energy [60]. Figure 10 shows the reverse I-V characteristics before and after irradiation and subsequent annealing, as well as the corresponding capacitance-voltage data used to extract carrier loss rates. Annealing at 300 °C produced a recovery of approximately half of the carriers in the $Ga_2O_3$, while annealing at

450 °C almost restored the reverse breakdown voltage [60]. The on/off ratio of the rectifiers was severely degraded by proton damage and was only partially recovered by 450 °C annealing. The minority carrier diffusion length decreased from ~340 nm in the starting material to ~315 nm after proton irradiation [61,62]. The reverse recovery characteristics showed little change, with values in the range 20-30 nsec before and after proton irradiation [63].

**(v) Trap States Induced by Proton Irradiation**

Figure 11 shows a compilation of trap states observed in as-grown and proton-irradiated $Ga_2O_3$. These states span a large portion of the gap [61,64-66]. Table II shows a summary of the origin, trap parameters and possible origin of these states. The trap assignations are still tentative in most cases [61,64-66].

Epitaxial films of β-$Ga_2O_3$ grown by hydride vapor phase epitaxy (HVPE) on native substrates exhibit deep electron traps near $E_c$-0.6 eV, $E_c$-0.75 eV, $E_c$-1.05 eV, similar to the E1, E2, and E3 electron traps observed in bulk β-$Ga_2O_3$ crystals [61,64-66]. The concentration of these traps in the HVPE films is 1-2 orders of magnitude lower than in bulk material [61]. Proton irradiation increased the density of E2 ($E_c$-0.75 eV) and $E_c$-2.3 eV traps, suggesting these incorporate native defects. Irradiation with 10-20 MeV protons creates deep electron and hole traps, a strong increase in photocapacitance and prominent persistent photocapacitance that partly persists above room temperature [61,62]. Typical DLTS spectra from samples before and after 10 MeV proton irradiation are shown in Figure 12, with the presence of a prominent electron trap near $E_c$-1.05 eV (capture cross section of $\sigma_n = 2 \times 10^{-12}$ cm$^2$) in the control sample. Two minor traps with levels $E_c$-0.6 eV ($\sigma_n = 5.6 \times 10^{-15}$ cm$^2$) and $E_c$-0.75 eV ($\sigma_n = 6.5 \times 10^{-15}$ cm$^2$) were also detected. After proton irradiation, the dominant peak in DLTS spectra was an electron trap with level $E_c$-0.75 eV (electron capture cross section $\sigma_n = 6.5 \times 10^{-15}$ cm$^2$), with a prominent shoulder

due to the $E_c$-1.05 eV electron trap. In the notation of Ref.64, these are respectively E1, E2, and E3 electron traps. The concentrations of E2 and E3 increased and a new trap E4 at $E_c$-1.2 eV emerged after proton irradiation. Figure 13 shows the variation of DLTS (top) and ODLTS (bottom) peak amplitude and shape as a function of rate windows for samples irradiated with 20 MeV protons.

Hole traps in the lower half of the bandgap were investigated using optical injection. Three hole-traps H1 (STH), H2 (ECB) and H3, with activation energies 0.2, 0.4, and 1.3 eV, respectively, were detected. The H1 (STH) feature was suggested to correspond to the transition of polaronic states of self-trapped holes (STH) to mobile holes in the valence band. The broad H2 (ECB) feature was assigned to overcoming of the electron capture barrier (ECB) of centers responsible for persistent photocapacitance at T< 250 K. The H3 peak was produced by detrapping of holes from $E_v$+(1.3-1.4) eV hole traps related to $V_{Ga}$ acceptors. A deep acceptor with optical ionization threshold near 2.3 eV is likely responsible for high temperature persistent photocapacitance surviving up to temperatures higher than 400 K. Table II summarizes reported trap states energy levels, capture cross sections and possible origin in as-grown and irradiated $Ga_2O_3$.

**(vi) Dominant Defect Induced by Proton Irradiation**

There is particular interest in the properties of hydrogen in $Ga_2O_3$ because of the predictions from density functional theory and total energy calculations that it should be a shallow donor in this material [34,67]. The generally observed n-type conductivity, therefore, may at least in part be explained by the presence of residual hydrogen from the growth ambient, rather than to native defects such as Ga interstitials or O vacancies, the latter of which are suggested to be deep donors [67-70]. There is some experimental support for the fact that hydrogen

may be a shallow donor in $Ga_2O_3$ from experiments on its muonium counterpart and from electron paramagnetic resonance of single-crystal samples [68].

Fourier Transform Infrared Spectroscopy studies on samples ion implanted with hydrogen or deuterium to obtain concentrations of ~$10^{20}$ $cm^{-3}$ was used to examine temperature- and polarization-dependent effects as well as relative H- and D- concentrations [71]. These results, coupled with detailed theoretical calculations, showed no evidence of interstitial atomic hydrogen ($H_i$); instead, the defects observed involve H trapped at a Ga vacancy, the primary member involving a particular two-H configuration. This configuration is shown in Figure 14 [71]. The dominant hydrogen or deuterium absorption lines appear at 3437 and 2545 $cm^{-1}$, respectively. Incorporation of $H_2$ and $D_2$ simultaneously, split these OH and OD lines into two lines. This requires the defects contains two equivalent H atoms. This, and the fact that the lines are completely polarized, leads to the model where two H atoms are bonded to a Ga vacancy. When the samples are implanted with hydrogen, additional absorption peaks are observed. As they are annealed, these defects become converted into the 3437 and 2545 $cm^{-1}$ lines at 400 °C. These lines are stable up to 700 °C, where they are then converted into other new lines [71].

**(vii) Electron Irradiation Damage**

1.5 MeV electron irradiation of vertical rectifiers fabricated on epi $Ga_2O_3$ on bulk β-$Ga_2O_3$ at fluences from 1.79 × $10^{15}$ to 1.43 × $10^{16}$ $cm^{-2}$ caused a reduction in carrier concentration in the $Ga_2O_3$, with a carrier removal rate of 4.9 $cm^{-1}$ [72-74]. This compares to a carrier removal rate of ~300 $cm^{-1}$ for 10 MeV protons in the same material. Figure 15 (top) shows the 2 kT region of the forward current-voltage characteristics increased due to electron-induced damage, with a more than 2 order of magnitude increase in on-state resistance at the highest fluence [72]. There was a

reduction in reverse current, which scaled with electron fluence. The on/off ratio at -10V reverse bias voltage was severely degraded by electron irradiation, decreasing from approximately $10^7$ in the un-irradiated reference diodes to approximately $2 \times 10^4$ for the highest fluence of $1.43 \times 10^{16}$ $cm^{-2}$. The changes in device characteristics were accompanied by a decrease in electron diffusion length from 325 to 240 μm at 300 K [74], as shown at the bottom of Figure 15. Time-resolved cathodoluminescence after 1.5 MeV electron irradiation showed a 210 ps decay lifetime and reduction in carrier lifetime with increased fluence [74].

**(viii) Alpha Particle Damage**

$Ga_2O_3$ rectifiers irradiated with 18 MeV alpha particles to a fluences of $10^{12}$-$10^{13}$ $cm^{-2}$, simulating space radiation exposure [75], exhibited carrier removal rate in the drift region of 406-728 $cm^{-1}$. These values are factors of 2-3 higher than for high energy (10 MeV) protons and two orders of magnitude higher than for 1.5 MeV electron irradiation of the same material. The reverse breakdown voltage increased in response to a reduction in channel carrier density (Figure 16) and the on/off ratio was also degraded. The on-state resistance of the rectifiers was more degraded by alpha particle irradiation than either ideality factor or barrier height.

**(ix) γ-Ray Damage**

Wong et al.[76] examined the gamma-ray irradiation tolerance of lateral depletion mode β-$Ga_2O_3$ MOSFETs to doses of 1.6 MGray ($SiO_2$), with little effect on output current and threshold voltage to this total dose. A dose of 1 Gray (Gy) corresponds to an absorbed radiation energy of 1 J per kg of mass, with $SiO_2$ being a common reference material. Degradation in the gate oxide were found to limit the overall radiation resistance [76].

**(x) X-Ray Damage**

Constant voltage stress of $\beta$-$Ga_2O_3$ MOS capacitors with $Al_2O_3$ gate dielectrics showed increasing electron-trap densities for increasingly positive stress voltages, and hole traps created for irradiation with 10 keV X-rays devices at a dose rate of 31.5 krad ($SiO_2$) $min^{-1}$ under grounded bias conditions [77]. Stress-induced traps were located primarily in the $Al_2O_3$ gate dielectric layer, and distributed broadly in energy. Oxygen vacancies in the $Al_2O_3$ were suggested to be most likely defects created [77]. The radiation-induced voltage shifts were comparable to or less than those of the MOSFETs exposed to gamma-rays discussed above [76].

Figure 17 shows a compilation of carrier removal rates in $Ga_2O_3$ for different types and energy of radiation. The data reported to date shows that the carrier removal rates in $Ga_2O_3$ are basically comparable to those reported previously for GaN [31-33,35,36].

**Conclusions**

The present review has comprehensively examined the radiation harness of a promising ultra-wide bandgap material, β-$Ga_2O_3$. Therefore, the radiation damage by high energy particle was investigated at both material and device level. The initial data on proton, electron, x-ray, gamma and neutron irradiation of β-$Ga_2O_3$ show fairly comparable radiation resistance to conventional wide bandgap semiconductors under the similar conditions. The carrier removal rates in irradiated rectifier structures range from ~5 $cm^{-1}$ for 1.5 MeV electrons to 730 $cm^{-1}$ for 18 MeV alpha particles. Thermal annealing at ~500 °C brings a significant recovery towards the initial, un-irradiated characteristics. The dominant defect formed in $Ga_2O_3$ by annealing in an $H_2$ ambient or by the implantation of protons is a specific relaxed $V_{Ga}$-2H structure for the 3437 $cm^{-1}$ line that dominates the infrared absorption spectra. There is significant scope for additional work to determine carrier removal rates at additional energies for each radiation type, to look for

dose-rate effects, SEU responses, the role of interfaces in MOS structures and annealing stages of the induced defects. In the latter case, it is of importance to know whether in-situ thermal annealing or forward biased minority carrier injection annealing are effective in $Ga_2O_3$ devices, since these could be used as simple refresh cycles for radiation damaged devices.

## ACKNOWLEDGMENTS

The work at Korea University was supported by Space Core Technology Development Program (2017M1A3A3A02015033) and the Technology Development Program to Solve Climate Changes (2017M1A2A2087351) through the National Research Foundation of Korea funded by the Ministry of Science, ICT and Future Planning of Korea. The work at UF is partially supported by HDTRA1-17-1-0011 (Jacob Calkins, monitor). The project or effort depicted is sponsored by the Department of the Defense, Defense Threat Reduction Agency. The content of the information does not necessarily reflect the position or the policy of the federal government, and no official endorsement should be inferred. The work at NUST MISiS was supported in part by the Ministry of Education and Science of the Russian Federation in the framework of Increase Competitiveness Program of NUST (MISiS) (K2-2014-055).

**Table I.** Generic radiation hardness requirements for microelectronics (adapted from Defense Threat Reduction Agency) (http://www.dtra.mil/Portals/61/Documents/Missions/DTRA%20StratPlan%202016-2020%20opt.pdf?ver=2016-03-23-135043-530)

| **Parameter** | **Ultimate Goal** | **Current Requirement** |
|---|---|---|
| Total Ionizing Dose (kRad (Si)) | $10^3$ | $3 \times 10^2$ |
| Single Event Upset (SEU) (errors/bit-day) | $< 10^{-11}$ | $<10^{-10}$ |
| Single Event Functional Interrupt (errors/chip-day) | none | $<10^{-5}$ |
| Single Event Latch-Up | none | none |
| Dose Rate Upset (radSi)/s | none | $>10^8$ |
| Displacement Damage (n/cm$^2$) | $10^{14}$ | $10^{12}$ |

**Table II.** Electron (E) or hole (H) traps in as-grown and irradiated material.

| **Trap notation** | **$E_a$ (eV)** | **$\sigma_n$ or $\sigma_p$($cm^2$)** | **Material or method** | **Induced by irradiation** | **Possible identity** |
|---|---|---|---|---|---|
| E1[78] | 0.55-0.62 | (3-30) × $10^{-14}$ | Bulk Sn doped[78], Bulk Si doped[64], HVPE Si doped[61] | 10 - 20 MeV protons, 18 MeV α-particles | unknown |
| E2[78] | 0.74-0.82 | (3-30) × $10^{-16}$ | Bulk Sn doped[78], bulk Si doped[64], HVPE Si doped[61,66], MBE Ge doped[79], FETs[80] | - | Fe[61,78,80] |
| E2*[66] | 0.75-0.79 | (3-7) × $10^{-14}$ | HVPE Si doped[61,66], FETs[80] | 0.8 MeV protons, 10 MeV protons, 20 MeV protons, 18 MeV a-particles | Native defect complex |
| E3[78] | 0.95-1 | (0.6-6) × $10^{13}$ | Bulk Sn doped[78], bulk Si doped[64], HVPE Si doped[61,66], MBE Ge doped[79] | 10 - 20 MeV protons, 18 MeV α-particles | unknown |
| E4[61] | 1.2 | (4-15) × $10^{-14}$ | | 10-20 MeV protons, 18 MeV α-particles | VO(III) |
| E5 | 0.18 | (1-7) × $10^{-19}$ | MBE Ge doped [79] | - | unknown |
| E6 | 0.21 | (0.2-2) × $10^{-15}$ | MBE Ge doped, MOCVD Sn doped [52] | - | unknown |
| E7[61,66] | 0.27-0.29 | 5.6 × $10^{-18}$ | HVPE Si doped | 20 MeV protons, 18 MeV α-particles | unknown |
| H1(STH) [81] | 0.2-0.3 | (2.3-14) × $10^{-15}$ | ODLTS [81] | HVPE Si doped as-grown, HVPE Si doped and irradiated with 20 MeV protons or 18 MeV α-particles | Self-trapped holes [81] |
| H3 | 1.3-1.4 | 2.9 × $10^{-12}$ | ODLTS, LCV, SSPC [81] | HVPE Si doped as grown, HVPE Si doped as grown and ted with 20 MeV protons and 18 MeV α-particles, | $V_{Ga}$ |

| | | | | | |
|---|---|---|---|---|---|
| | | | | MOCVD Sn doped | |
| H4 | | | DLOS[64,79], LCV, SSPC[52,61,81] | Bulk Si doped, MBE Ge doped, MOCV Sn doped, neutron irradiated, 10-20 MeV proton irradiated, 18 MeV a-particles | unknown |
| H5 | | | DLOS [79], LCV, SSPC[52,61,81] | MBE Ge doped | Possibly same as H3[81] |
| H6 | | | DLOS[64,79] | Bulk Si doped, MBE Ge doped, neutron irradiated | Possibly same as H1(STH) |
| H7 | | | DLOS [79] | MBE Ge doped | Possibly same as E2* [61,81] |

$\alpha_p$ calculated from ODLTS Arrhenius plot assuming hole effective mass equal to 1

LCV is CV characteristics with monochromatic light excitation, SSPC is steady state photocapacitance, ODLTS is deep level transient spectroscopy with optical excitation, DLOS is deep level optical spectroscopy

**References**

1. J.Y. Tsao, S. Chowdhury, M.A. Hollis, D. Jena, N.M. Johnson, K.A. Jones, R.J. Kaplar, S. Rajan, C.G. Van de Walle, E. Bellotti, C.L. Chua, R. Collazo, M.E. Coltrin, J.A. Cooper, K.R. Evans, S. Graham, T.A. Grotjohn, E.R. Heller, M. Higashiwaki, M.S. Islam, P.W. Juodawlkis, M.A. Khan, A.D. Koehler, J.H. Leach, U.K. Mishra, R.J. Nemanich, R.C.N. Pilawa-Podgurski, J.B. Shealy, M.J. Tadjer, A.F. Witulski, M. Wraback and J.A. Simmons, Advanced Electronic Mater., 2018, 4, 1600501, https://doi.org/10.1002/aelm.201600501

2. Akito Kuramata, Kimiyoshi Koshi, Shinya Watanabe, Yu Yamaoka, Takekazu Masui, and Shigenobu Yamakoshi, Jpn. J. Appl. Phys. 2016, 55, 1202A2-1

3. H. Von Wenckstern, Adv. Electron. Mater. 2017, 3, 1600350.

4. Michael A. Mastro, Akito Kuramata, Jacob Calkins, Jihyun Kim, Fan Ren, and S. J. Pearton, ECS J. Solid State Sci. Technol, 2017, 6, P356.

5. M.J. Tadjer, M.A. Mastro, N.A. Mahadik, M. Currie, V.D. Wheeler, J.A. Freitas, Jr., J.D. Greenlee, J.K. Hite, K.D. Hobart, C.R. Eddy, Jr. and F.J. Kub, J. Electr. Mater. 2016, 45, 2031.

6. Burhan Bayraktaroglu, Assessment of $Ga_2O_3$ Technology, Air Force Research Lab, Devices for Sensing Branch, Aerospace Components & Subsystems Division, Report AFRL-RY-WP-TR-2017-0167 (2017). http://www.dtic.mil/dtic/tr/fulltext/u2/1038137.pdf

7. S.I. Stepanov, V.I. Nikolaev, V.E. Bougrov and A.E. Romanov, Rev. Adv. Mater. Sci., 2016, 44, 63.

8. Subrina Rafique, Lu Han, and Hongping Zhao, ECS Transactions, 2017, 80, 203.

9. S.J. Pearton, Jiancheng Yang, Patrick H. Cary IV, F. Ren, Jihyun Kim, Marko J. Tadjer and Michael A. Mastro, App. Phys. Rev., 2018, 5, 011301.

10. Masataka Higashiwaki and Gregg H. Jessen, Appl. Phys. Lett. 2018, 112, 060401, 10.1063/1.5017845

11. Andrew M. Armstrong, Mary H. Crawford, Asanka Jayawardena, Ayayi Ahyi, and Sarit Dhar, J. Appl. Phys., 2016, 119, 103102.

12. J. Kim, S. Oh, M. A. Mastro and J. Kim, Phys. Chem. Chem. Phys., 2016, 18, 15760.

13. M. Kim, J.-H. Seo, U. Singisetti and Z. Ma, J. Mater. Chem. C, 2017, 5, 8338.

14. D. Gogova, G. Wagner, M. Baldini, M. Schmidbauer, K. Irmscher, R. Schewski, Z. Galazka, M. Albrecht, R. Fornari, J. Cryst. Growth, 2014, 401, 665.

15. D. Gogova, M. Schmidbauer and A. Kwasniewski, Cryst. Eng. Comm, 2015, 17, 6744.

16. E. Chikoidze, A. Fellous, A. Perez-Tomas, G. Sauthier, T. Tchelidze, C.Ton-That, T. T. Huynh, M. Phillips, S. Russell, M. Jennings, B. Berini, F. Jomard, Y. Dumont, Materials Today Phys, 2017, 3, 118.

17. J. Kim, M. A. Mastro, M. J. Tadjer and J. Kim, ACS Appl. Mater. Interf, 2017, 9, 21322.

18. G. Yang, S. Jang, F. Ren, S. J. Pearton and J. Kim, ACS Appl. Mater. Interf, 2017, 9, 40471.

19. Zbigniew Galazka, Reinhard Uecker, Detlef Klimm, Klaus Irmscher, Martin Naumann, Mike Pietsch, Albert Kwasniewski, Rainer Bertram, Steffen Ganschow, and Matthias Bickermann, ECS J. Solid State Sci. Technol., 2017 ,6, Q3007.

20. Michele Baldini, Martin Albrecht, Andreas Fiedler, Klaus Irmscher, Robert Schewski, and Günter Wagner, ECS J. Solid State Sci. Technol. 2017, 6, Q3040.

21. S. Rafique, L. Han, M.J. Tadjer, J.A. Freitas Jr, N.A. Mahadik and H. Zhao, Appl. Phys. Lett., 2016, 108, 182105-1.

22. J. F. Ziegler and W. A. Lanford, Science, 1979, 206, 776.

23. J.S. Melinger, S. Buchner, D. McMorrow, W.J. Stapor, T.R. Weatherford, A.B. Campbell and H. Eisen, IEEE Trans Nucl. Sci., 1994, 41, 2574, doi: 10.1109/23.340618

24. E. Normand, IEEE Trans. Nucl. Sci, 1996, 43, 461, doi: 10.1109/23.490893

25. Sophie Duzellier, Aerospace Sci. Technology, 2005, 9, 93, https://doi.org/10.1016/ j.ast. 2004.08.006

26. F.W. Sexton, IEEE Trans Nucl. Sci, 2003, 50, 603, doi: 10.1109/TNS.2003.813137

27. Edward Petersen, Single Event Effects in Aerospace (John Wiley & Sons, NY, 2011).

28. J. F. Ziegler, M. D. Ziegler, J. P. Biersack, Nucl. Instrum. Methods Phys. Res. B Beam Interact. Mater. At., 2010, 268, 1818.

29. J. R. Srour and J. W. Palko, IEEE Trans. Nucl. Sci., 2006, 53, 3610.

30. J. Nord, K. Nordlund and J. Keinonen, Phys. Rev. B, 2003, 68, 184104.

31. S.J. Pearton, Y.- S. Hwang and F. Ren, J. Mater.2015, 67, 1601.

32. A. Ionascut-Nedelcescu, C. Carlone, A. Houdayer, H.J. von Bardeleben, J.-L. Cantin, and S. Raymond, IEEE Trans. Nucl. Sci., 2002, 49, 2733.

33. B.D. Weaver, T.J. Anderson, A.D. Koehler, J.D. Greenlee, J.K. Hite, D.I. Shahin, F.J. Kub and K.D. Hobart, ECS J. Solid State Sci. Technol. 2016, 5, Q208.

34. J.B. Varley, J. R. Weber, A. Janotti and C.G. Van de Walle, Appl. Phys. Lett., 2010, 97, 142106-1.

35. A.Y. Polyakov, S.J. Pearton, P. Frenzer, F. Ren, L. Liu and J. Kim, J. Mater. Chem. C, 2013, 1, 877.

36. S. J. Pearton, R. Deist, F. Ren, L. Liu, A. Y. Polyakov and J. Kim, J. Vac. Sci. Technol. A, 2013, 31, 050801.

37. L. N. Cojocaru, Radiation Effects, 1974, 21, 157, DOI:10.1080/00337577408241456.

38. Cameron L. Tracy, Maik Lang, Daniel Severin, Markus Bender, Christina Trautmann, Rodney C. Ewing, Nucl. Instr. Meth. Physics Research B, 2016, 374, 40.

39. see the extensive database of The NASA Goddard Space Flight Center Radiation Effects effort, https://radhome.gsfc.nasa.gov/

40. E.G. Stassinopoulos, G.J. Brucker, D.W. Nakamura, C.A. Stauffer, G.B. Gee, J.L. Barth, IEEE Trans. Nuclear Sci., 1996, 43, 369.

41. Michael J. Campola, Donna J. Cochran, Shannon Alt, Alvin J. Boutte, Dakai Chen, Robert A. Gigliuto, Kenneth A. LaBel, Jonathan A. Pellish, Raymond L. Ladbury, Megan C. Casey, Edward P. Wilcox, Martha V. O'Bryan, Jean-Marie Lauenstein, Michael A. Xapsos, Compendium of Total Ionizing Dose and Displacement Damage Results from NASA Goddard Spaceflight Center, 2016 IEEE Radiation Effects Data Workshop (REDW), Portland, Oregon 11-15 July 2016, pp. 1-9, ISBN: 978-1-5090-5114-4

42. T. R. Oldham, K. W. Bennett, J. Beaucour, T. Carriere, C. Polvey and P. Garnier, IEEE Trans. Nucl. Sci., 1993, 40, 1820.

43. P. E. Dodd, F. W. Sexton, and P. S. Winokur, IEEE Trans. Nucl. Sci., 1994, 41, 2005

44. L. Scheick, IEEE Trans. Nuclear Sci, 2014, 61, 2881

45. A.P. Karmarkar, B.D. White, D. Buttari, D.M. Fleetwood, R.D. Schrimpf, R. A. Weller, L.J. Brillson and U.K. Mishra, IEEE Trans. Nucl. Sci., 2005, 52 2239.

46. S. J. Pearton, F. Ren, Erin Patrick, M. E. Law and Alexander Y. Polyakov, ECS J. Solid State Sci. Technol., 2016, 5, Q35.

47. courtesy of Jacob Calkins, Defense Threat Reduction Agency, http://www.dtra.mil/Research/Basic-and-Applied-Science/

48. E. Korhonen, F. Tuomisto, D. Gogova, G. Wagner, M. Baldini, Z. Galazka, R. Schewski, M. Albrecht, Appl. Phys. Lett. 2015, 106, 242103.

49. B. E. Kananen, L. E. Halliburton, K. T. Stevens, G. K. Foundos, K. B. Chang, and N. C. Giles, Appl. Phys. Lett.2017,110, 202104

50. B. E. Kananen, N. C. Giles, L. E. Halliburton, G. K. Foundos, K. B. Chang, and K. T. Stevens, J. Appl. Phys.2017, 122, 215703. https://doi.org/10.1063/1.5007095

51. A. Kyrtsos, M. Matsubara, and E. Bellotti, Phys. Rev. B 95, 245202 (2017). https://doi.org/10.1103/PhysRevB.95.245202

52. A.Y. Polyakov, N.B. Smirnov, I.V. Shchemerov, D. Gogova, S.A. Tarelkin and S.J. Pearton, J. Appl. Phys. 2018, 123,115702.

53. E. Wendler, E. Treiber, J. Baldauf, S. Wolf and C. Ronnig, Nucl. Instr. Meth Physics Res. B, 2016, 379, 85.

54. Linpeng Dong, Renxu Jia, Chong Li, Bin Xin, Yuming Zhang, J. Alloys Compounds, 2017, 712, 379, https://doi.org/10.1016/j.jallcom.2017.04.020

55. A. A. Arehart, E. Farzana, T. E. Blue and S.A. Ringel, presented at 2nd International Workshop on $Ga_2O_3$ and Related Materials, Parma, Italy, September 2017.

56. S. Ringel et al., "The presence and impact of deep level defects induced by high energy neutron radiation in beta-phase gallium oxide", GOMACTech, Mar. 2018.

57. D. Szalkai, Z. Galazka, K. Irmscher, P. Tüttő, A. Klix and D. Gehre, IEEE Trans. Nucl. Sci., 2017, 64, 1574.

58. Max F. Chaiken and Thomas E. Blue, IEEE Trans. Nuclear Sci, 2018, 65, 1147.

59. Jiancheng Yang, F. Ren, Rohit Khanna, Kristen Bevlin, D. Geerpuram, Li-Chun Tung, J. Lin, H.X. Jiang, J. Lee, E. Flitsiyan, L. Chernyak, S. J. Pearton and A. Kuramata, J. Vac. Sci. Technol. B, 2017, 35, 051201.

60. J. Yang, Zhiting Chen, F.Ren, S. J. Pearton, Gwangseok Yang, Jihyun Kim, J. Lee, Elena Flitsiyan and Leonid Chernyak and A. Kuramata, J. Vac. Sci. Technol. B, 2018, 36, 011206.

61. A.Y. Polyakov, N.B. Smirnov, I.V. Shchemerov, E.B. Yakimov, Jiancheng Yang, F. Ren, G. Yang, Jihyun Kim, A. Kuramata and S. J. Pearton, Appl. Phys. Lett. 2018, 112, 032107.

62. E. B. Yakimov, A. Y. Polyakov, N. B. Smirnov, I. V. Shchemerov, Jiancheng Yang, F. Ren, Gwangseok Yang, Jihyun Kim and S. J. Pearton, J. Appl. Phys.2018, 123, 185704.

63. S. Ahn, Y.-H. Lin, F. Ren, S. Oh, Y. Jung, G. Yang, J. Kim, M. A. Mastro, J. K. Hite, C. R. Eddy, Jr. and S. J. Pearton, J. Vac. Sci. Technol. B, 2016, 34, 041213.

64. Z. Zhang, E. Farzana, A. R. Arehart, and S. A. Ringel, Appl. Phys. Lett., 2016, 108, 052105, https://doi.org/10.1063/1.4941429

65. Yoshitaka Nakano, ECS J Solid State Sci. Technology, 2017, 6, P615

66. M. E. Ingebrigtsen, J. B. Varley, A. Yu. Kuznetsov, B. G. Svensson, G. Alfieri, A. Mihaila, U. Badstübner, and L.Vines, Appl. Phys. Lett.,2018, 112, 042104, https://doi.org/10.1063/1.5020134

67. A. Janotti and C.G. Van de Walle, Nature Mater. 2007, 6, 44.

68. P.D.C. King and T.D. Veal, J. Phys. Condens. Matter 2011, 23, 334214.

69. S. Ahn, F. Ren, E. Patrick, M.E. Law, S. J. Pearton and A. Kuramata, Appl. Phys. Lett. 2016, 109, 242108.

70. S. Ahn, F. Ren, Erin Patrick, Mark E. Law and S. J. Pearton, ECS J. Solid State Sci. Technol.,2017,6, Q3026.

71. Philip Weiser, Michael Stavola, W. Beall Fowler, Ying Qin and S.J. Pearton, Appl. Phys. Lett. 112, 232104 (2018).

72. J. Yang, F. Ren, S.J. Pearton, G. Yang, J. Kim and A. Kuramata, J. Vac. Sci. Technol. B, 2017,35, 031208.

73. J. Lee, E. Flitsiyan, L. Chernyak, S. Ahn, F. Ren, L. Yun, S. J. Pearton, J. Kim, B. Meyler, and J. Salzman, ECS J. Solid State Sci. Technol. 2017, 6, Q3049.

74. J. D. Lee, Elena Flitsiyan, Leonid Chernyak, Jiancheng Yang, Fan Ren, S. J. Pearton, Boris Meyler and Y. Joseph Salzman, Appl. Phys. Lett.2018, 112, 082104.

75. Jiancheng Yang, Chaker Fares, Yu Guan, F. Ren, S. J. Pearton, Jinho Bae, Jihyun Kim and Akito Kuramata, J.Vac. Sci. Technol. B.2018, 36, 031205.

76. M.H. Wong, A. Takeyama, T. Makino, T. Ohshima, K. Sasaki, A. Kuramata, S. Yamakoshi, and M. Higashiwaki, Appl. Phys. Lett., 2018, 112, 023503, https://doi.org/10.1063/1.5017810

77. Maruf A. Bhuiyan, Hong Zhou, Rong Jiang, En Xia Zhang, Daniel M. Fleetwood, Peide D. Ye and Tso-Ping Ma, IEEE Electron Dev. Lett., 2018, 39, 1022

78. K. Irmscher, Z. Galazka, M. Pietsch, R. Uecker, and R. Fornari, J. Appl. Phys, 2011, 110, 063720

79. Esmat Farzana, Elaheh Ahmadi, James S. Speck, Aaron R. Arehart, and Steven A. Ringel, J. Appl. Phys, 2018, 123, 161410.

80. J. F. McGlone, Z, Xia, Yuewei Zhang, C. Joishi, Saurabh Lodha, Siddharth Rajan, Steven A. Ringel,and Aaron R. Arehart, IEEE Electron. Dev. Lett, 2018, 39, 1042.

81. A.Y. Polyakov, N.B. Smirnov, I.V. Shchemerov, S.J. Pearton, F. Ren, A. V. Chernykh, P.B. Lagov, and T.V. Kulevoy, to be published in APL Materials, 2019.

**Figure Captions**

**Figure 1** Breakdown voltages and on-state resistances for power electronic devices fabricated on different semiconductors (top) and schematic of bandgaps and equivalent wavelengths spanned by the range of compositions of both the GaN and $Ga_2O_3$-based family of materials with their associated Al and In-containing ternary alloys (bottom).

**Figure 2** (a) β-$Ga_2O_3$ crystal structure and (b) (010) and $(\bar{2}01)$ surfaces. Reprinted with permission from Pearton et al.,[9]. Copyright 2018, American Institute of Physics.

**Figure 3** Schematic of space radiation effects in the magnetosphere, Space Environments & Effects Program, NASA Marshall Space Flight Center http://holbert.faculty.asu.edu/eee560/spacerad.html

**Figure 4** Range of protons and alpha particles in $Ga_2O_3$ as a function of energy (1-100 MeV).

**Figure 5** Vacancy distributions calculated by SRIM in $Ga_2O_3$ for 10 or 20 MeV protons and 18 MeV alpha particles (top) and expanded view in the region relevant for devices (bottom)

**Figure 6** Model of the doubly ionized gallium vacancy in β-$Ga_2O_3$. An unpaired spin (the hole) is localized in a $p_z$ orbital on a threefold oxygen ion, O(II), adjacent to a gallium vacancy (dashed square) at a sixfold Ga(II) site. Reprinted with permission from Kananen et al [49], copyright 2017 American Institute of Physics.

**Figure 7** Schematic of O and Ga defects in $Ga_2O_3$ lattice. The Ga, O and N atoms are demonstrated by brown, red and blue spheres, respectively. Number 1 and 2 represent the vacancy sites of O and Ga, respectively. The yellow sphere labelled with number 3 denotes the interstitial sites for both O and Ga. Reprinted with permission from Dong et al. [54], copyright 2017, Elsevier.

**Figure 8** Group-wise displacement damage cross sections for neutron irradiation of $Ga_2O_3$. Reprinted with permission from Chaiken and Blue[58], copyright 2018, IEEE.

**Figure 9** Output characteristics ($I_{DS}$ vs. $V_{DS}$) of β-$Ga_2O_3$ nanobelt FET before and after 10 MeV proton irradiation at different doses: (a) as-fabricated, (b) $1 \times 10^{15}$ $cm^{-2}$, and (c) $2 \times 10^{15}$ $cm^{-2}$, (d) transfer characteristics ($I_{DS}$ vs. $V_{GS}$) of β-$Ga_2O_3$ nanobelt FET at $V_{DS}$ = 30 V before and after 10 MeV proton irradiation at different doses. Reprinted with permission from Yang et al. [18], copyright 2017, American Chemical Society.

**Figure 10** Reverse current density-voltage characteristics from rectifiers before and after 10 MeV proton irradiation with fluence of $10^{14}$ and then annealed at either 300 or 450°C (top). $C^{-2}$-V characteristics of $Ga_2O_3$ rectifiers before and after proton irradiation and subsequent annealing at either 300 or 450 °C (bottom). Reprinted with permission from Yang et al.[60], copyright 2108, American Institute of Physics.

**Figure 11** Schematic of energy levels in the gap of as–grown and proton irradiated $Ga_2O_3$.

**Figure 12** (a) DLTS spectra for β-$Ga_2O_3$ epilayers (b) high temperature DLTS spectra, before (red line) and after (blue line) proton irradiation. Reprinted with permission from Polyakov et al.[61], copyright 2018, American Institute of Physics.

**Figure 13** (top) DLTS spectra of $Ga_2O_3$ rectifiers after 20 MeV proton fluence of $10^{14}$ $cm^{-2}$, bias -1 V, pulse +1 V, $t_p$=3 s, showing variation of electron trap peaks with different rate windows; (bottom) ODLTS spectra after irradiation with fluence $10^{14}$ $cm^{-2}$, bias -1V, 259.4 nm LED, $t_p$=5 s, showing variation of hole trap signal with rate window settings.

**Figure 14** Schematic of $V_{Ga}$-2H defect in proton irradiated $Ga_2O_3$. Reprinted with permission from Weiser et al.[71], copyright 2018, American Institute of Physics.

**Figure 15** (a) I-Vs from $Ga_2O_3$ diodes before and after 1.5 MeV electron irradiation to different doses (b) diffusion length of electrons as a function of temperature after different electron irradiation doses. Reprinted with permission from Yang et al. [72], copyright 2018, American Institute of Physics.

**Figure 16** Reverse I-Vs from $Ga_2O_3$ rectifiers before and after 18 MeV alpha particle damage, along with summary of changes in device properties. Reprinted with permission from Yang et al. [75], copyright 2018, American Institute of Physics.

**Figure 17** Carrier removal rate in $Ga_2O_3$ as a function of energy for different types of radiation. Data is either from University of Florida (UF) [60,72,75], National University of Science and Technology (UST-MISiS) or Ohio State University (OSU) [55,56].

**Figure 1**

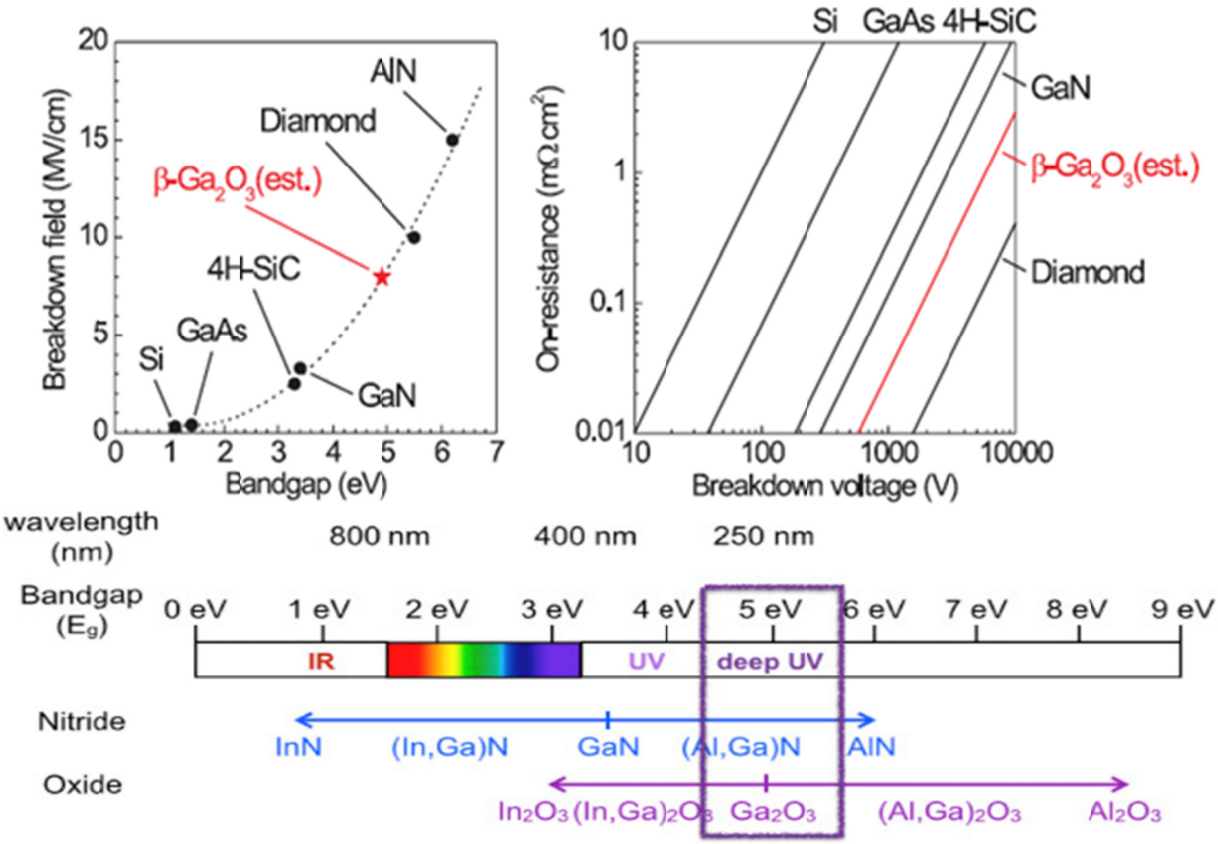
Breakdown field (MV/cm)
Bandgap (eV)
AlN
Diamond
β-Ga2O3(est.)
4H-SiC
GaAs
Si
GaN
On-resistance (mΩ.cm2)
Breakdown voltage (V)
Si GaAs 4H-SiC
GaN
β-Ga2O3(est.)
Diamond
wavelength (nm)
800 nm
400 nm
250 nm
Bandgap (Eg)
0 eV 1 eV 2 eV 3 eV 4 eV 5 eV 6 eV 7 eV 8 eV 9 eV
IR
UV
deep UV
Nitride
InN (In,Ga)N GaN (Al,Ga)N AlN
Oxide
In2O3 (In,Ga)2O3 Ga2O3 (Al,Ga)2O3 Al2O3

**Figure 2**

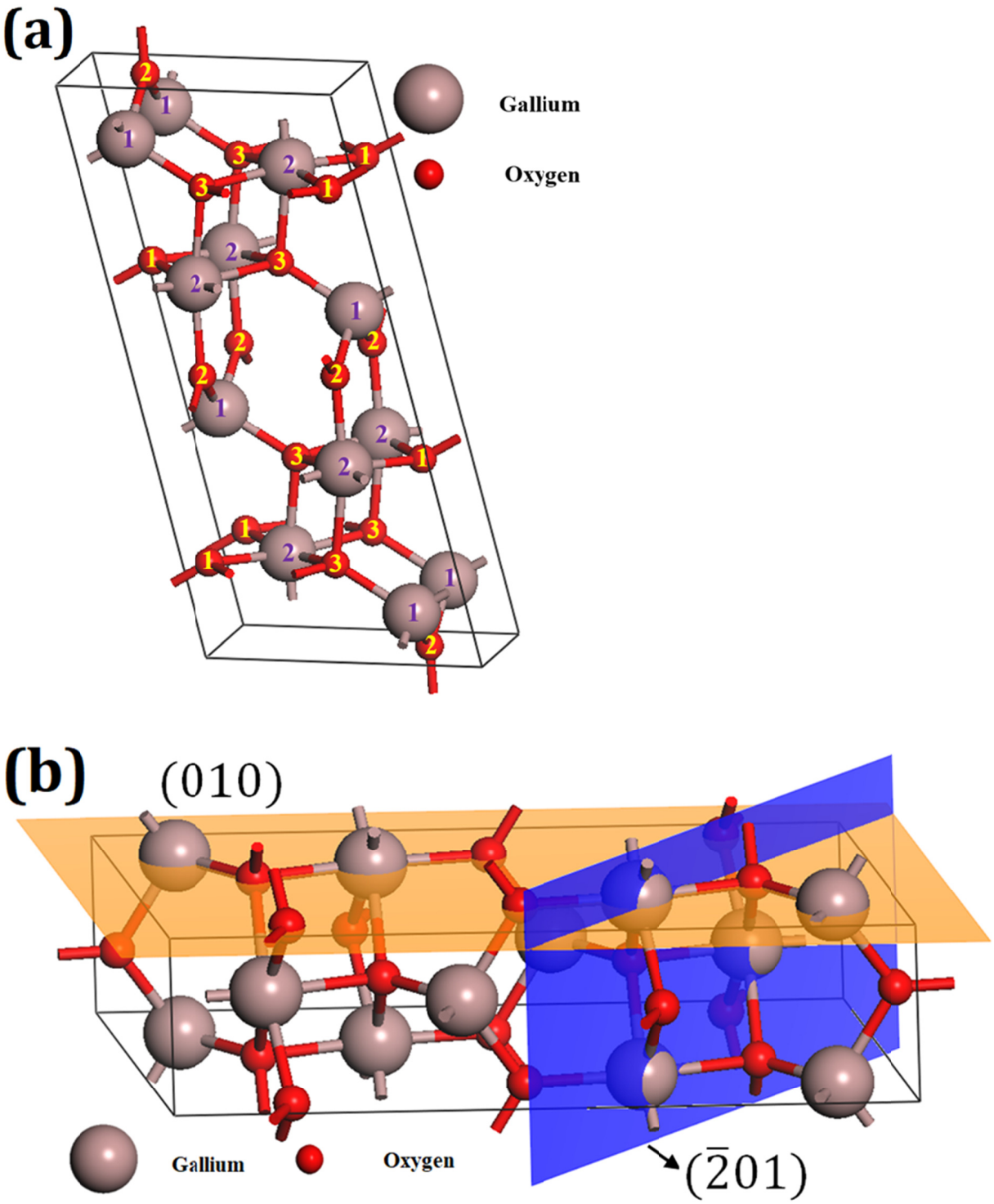

**Figure 3**

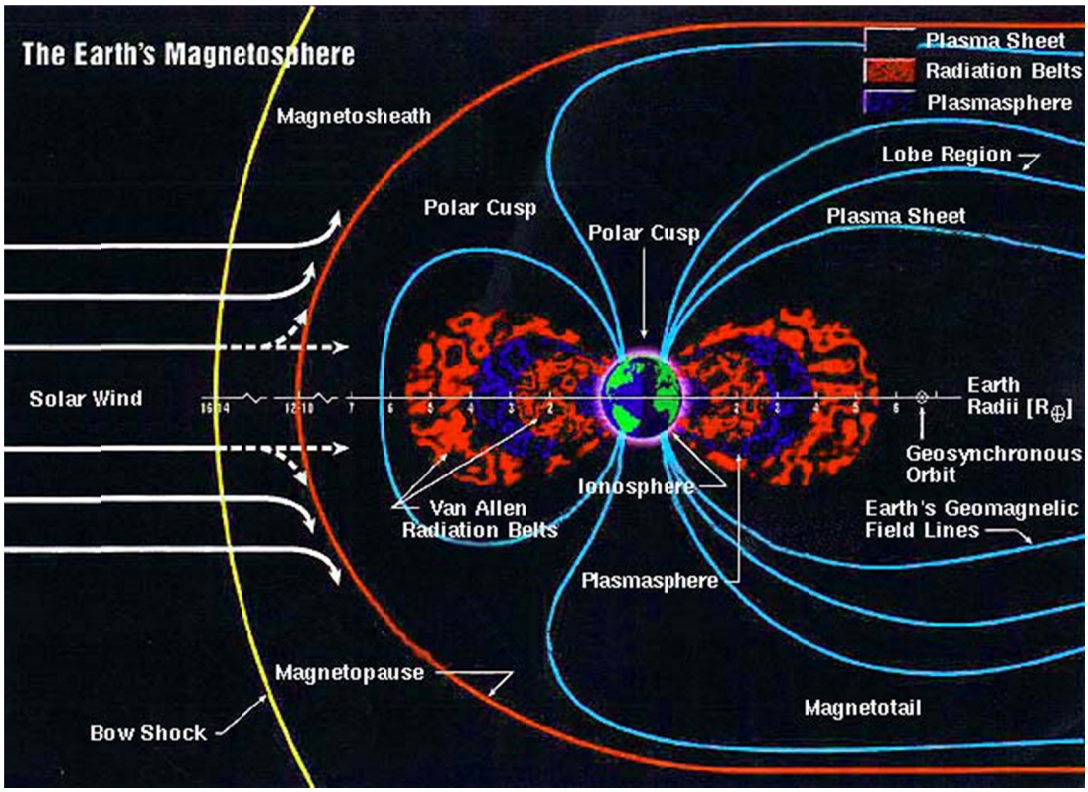
The Earth's Magnetosphere
Plasma Sheet
Radiation Belts
Plasmasphere
Magnetosheath
Lobe Region
Polar Cusp
Polar Cusp
Plasma Sheet
Solar Wind
Earth Radii [R⊕]
Geosynchronous Orbit
Ionosphere
Van Allen Radiation Belts
Earth's Geomagnelic Field Lines
Plasmasphere
Magnetopause
Bow Shock
Magnetotail

**Figure 4**

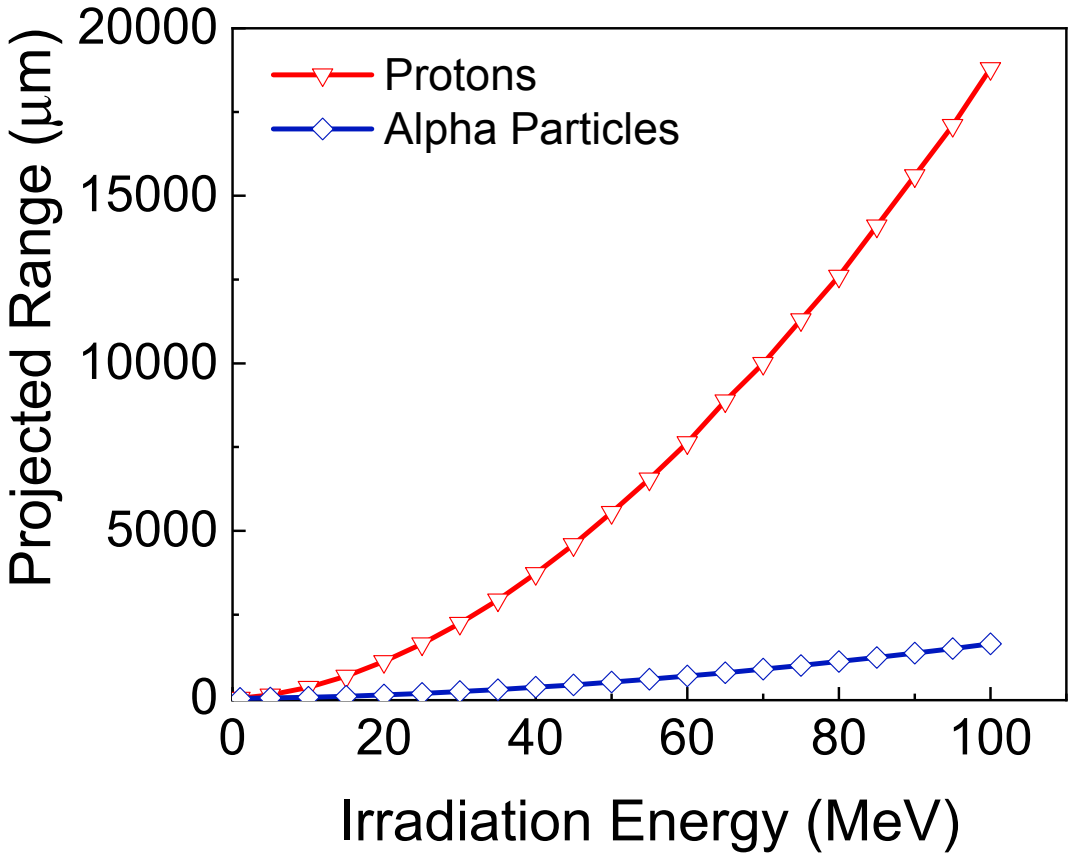
Projected Range (μm)
20000
15000
10000
5000
0
0
20
40
60
80
100
Irradiation Energy (MeV)
Protons
Alpha Particles

**Figure 5**

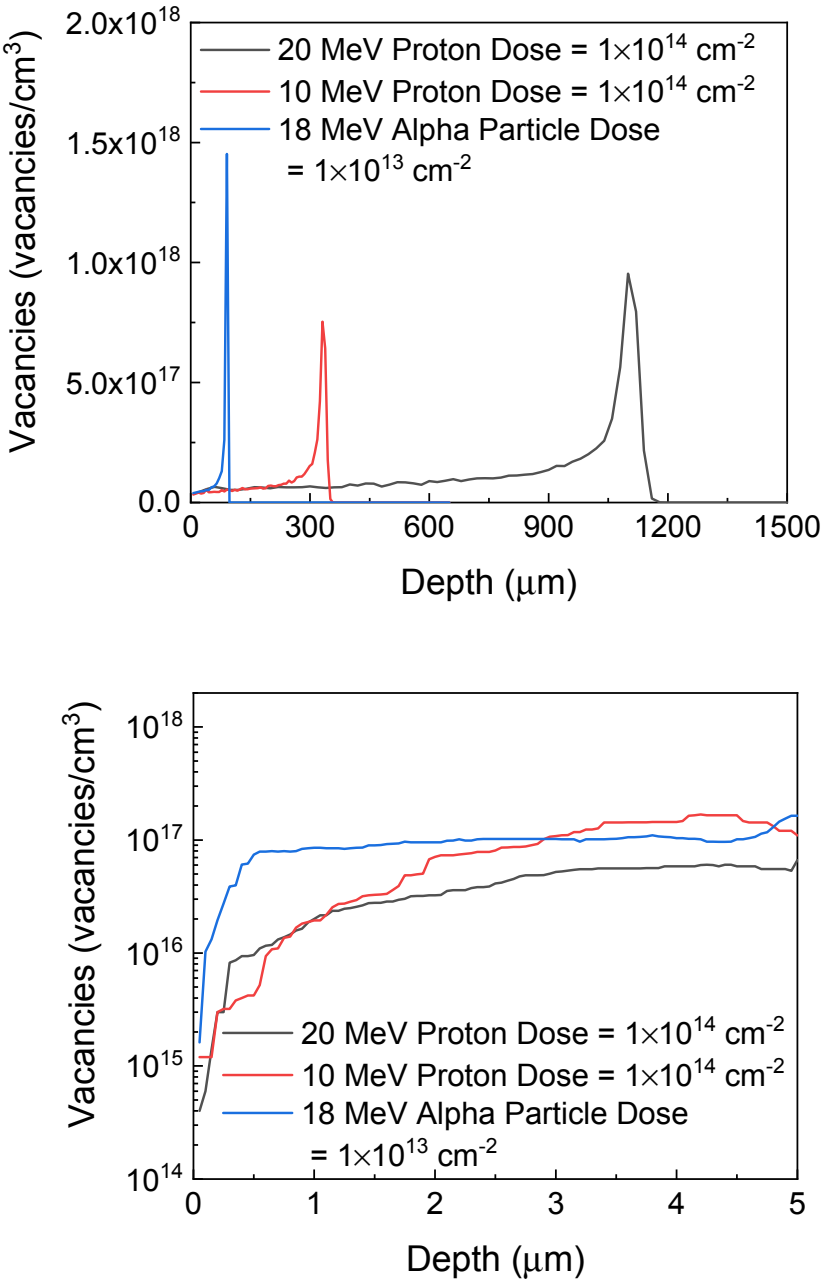
Vacancies (vacancies/cm$^3$)
2.0x10$^{18}$
1.5x10$^{18}$
1.0x10$^{18}$
5.0x10$^{17}$
0.0
0
300
600
900
1200
1500
Depth (μm)
20 MeV Proton Dose = 1×10$^{14}$ cm$^{-2}$
10 MeV Proton Dose = 1×10$^{14}$ cm$^{-2}$
18 MeV Alpha Particle Dose
= 1×10$^{13}$ cm$^{-2}$
Vacancies (vacancies/cm$^3$)
10$^{18}$
10$^{17}$
10$^{16}$
10$^{15}$
10$^{14}$
0
1
2
3
4
5
Depth (μm)
20 MeV Proton Dose = 1×10$^{14}$ cm$^{-2}$
10 MeV Proton Dose = 1×10$^{14}$ cm$^{-2}$
18 MeV Alpha Particle Dose
= 1×10$^{13}$ cm$^{-2}$

**Figure 6**

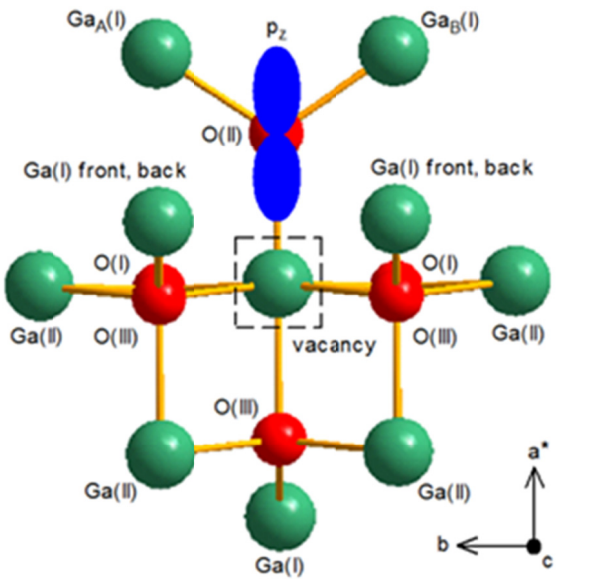
Ga$_A$(I)
p$_z$
Ga$_B$(I)
O(II)
Ga(I) front, back
Ga(I) front, back
O(I)
O(I)
Ga(II)
O(III)
vacancy
O(III)
Ga(II)
O(III)
Ga(II)
Ga(II)
Ga(I)
a*
b
c

**Figure 7**

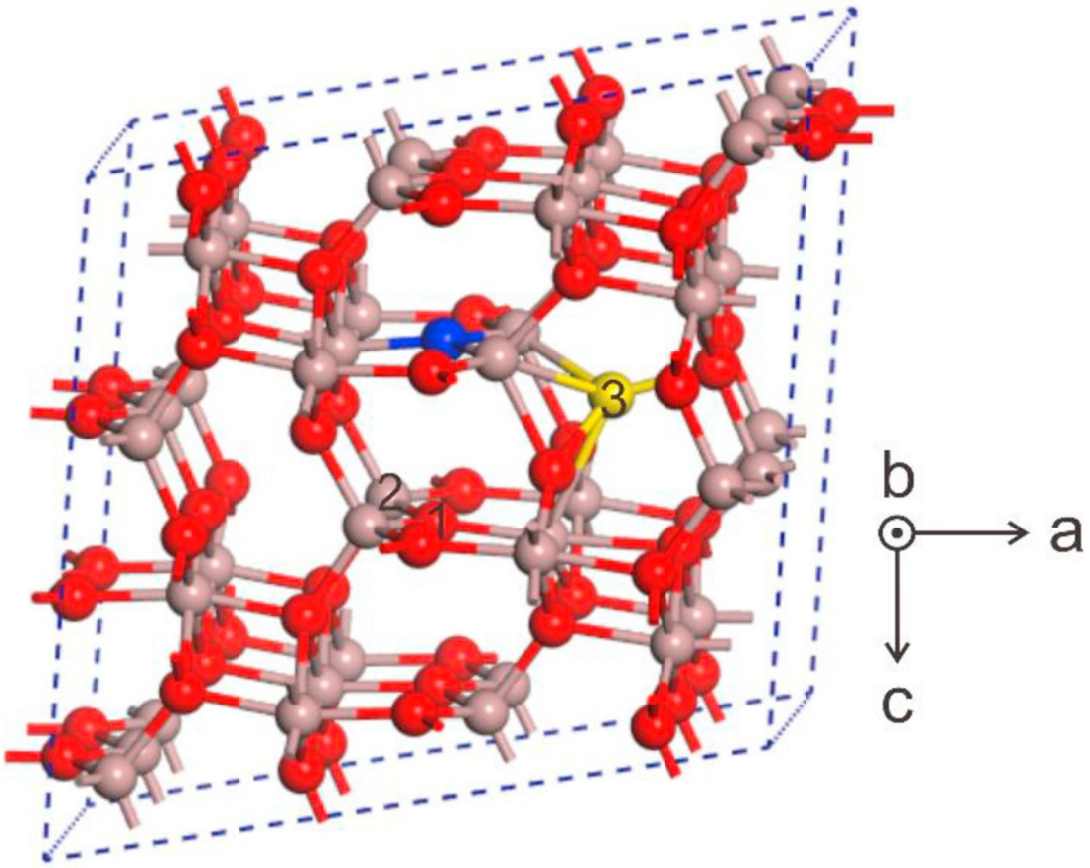

**Figure 8**

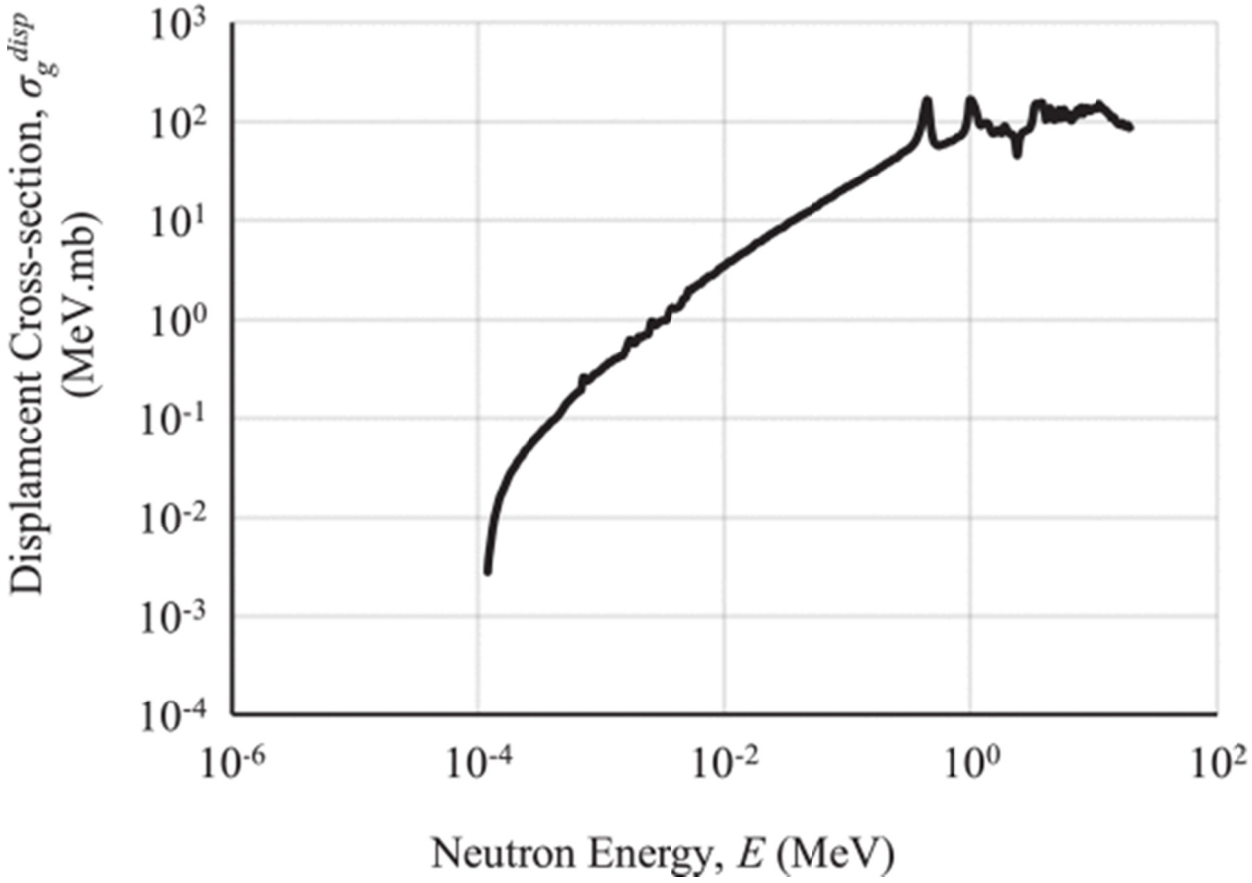
Displamcent Cross-section, $\sigma_g^{disp}$ (MeV.mb)
$10^3$
$10^2$
$10^1$
$10^0$
$10^{-1}$
$10^{-2}$
$10^{-3}$
$10^{-4}$
$10^{-6}$
$10^{-4}$
$10^{-2}$
$10^0$
$10^2$
Neutron Energy, $E$ (MeV)

**Figure 9**

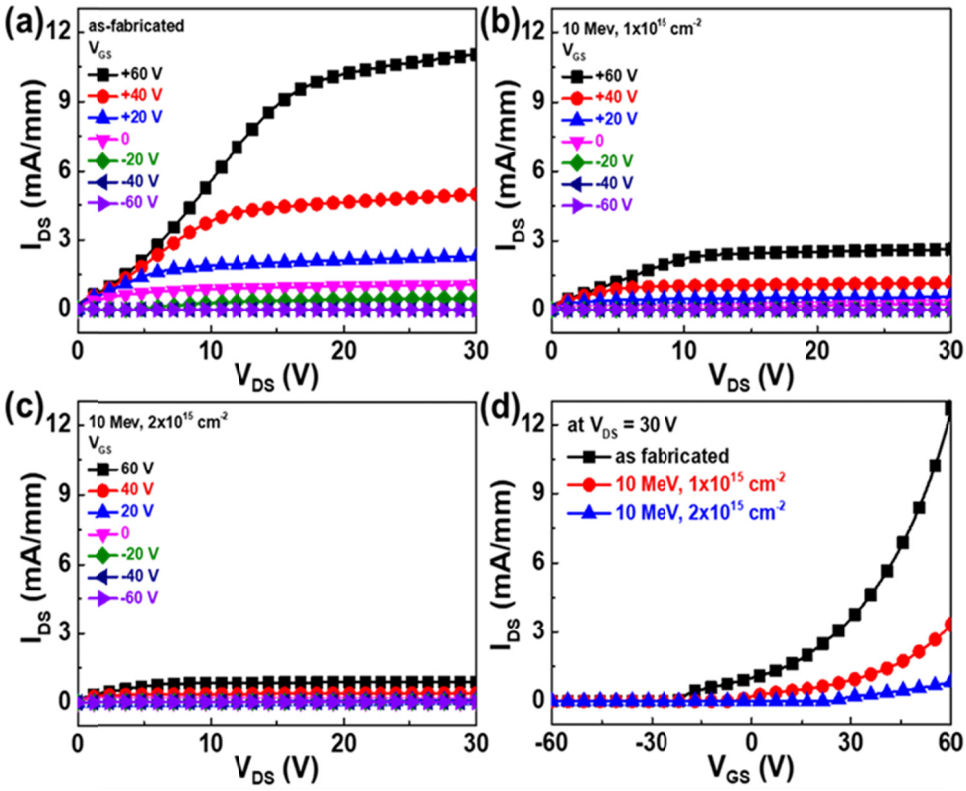
(a)
as-fabricated
$V_{GS}$
+60 V
+40 V
+20 V
0
-20 V
-40 V
-60 V
$I_{DS}$ (mA/mm)
$V_{DS}$ (V)
(b)
10 Mev, 1x10$^{15}$ cm$^{-2}$
$V_{GS}$
+60 V
+40 V
+20 V
0
-20 V
-40 V
-60 V
$I_{DS}$ (mA/mm)
$V_{DS}$ (V)
(c)
10 Mev, 2x10$^{15}$ cm$^{-2}$
$V_{GS}$
60 V
40 V
20 V
0
-20 V
-40 V
-60 V
$I_{DS}$ (mA/mm)
$V_{DS}$ (V)
(d)
at $V_{DS}$ = 30 V
as fabricated
10 MeV, 1x10$^{15}$ cm$^{-2}$
10 MeV, 2x10$^{15}$ cm$^{-2}$
$I_{DS}$ (mA/mm)
$V_{GS}$ (V)

**Figure 10**

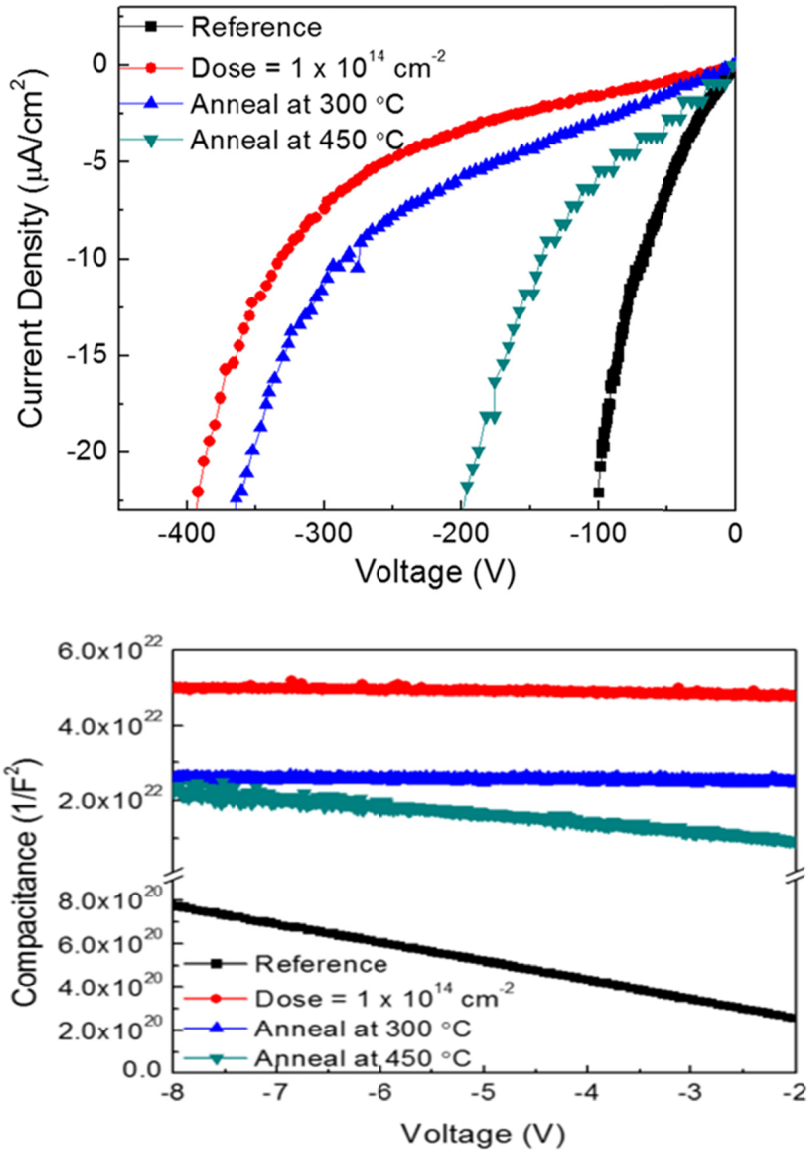
Reference
Dose = 1 x 10^14 cm^-2
Anneal at 300 °C
Anneal at 450 °C
Current Density (μA/cm^2)
0
-5
-10
-15
-20
-400
-300
-200
-100
0
Voltage (V)
6.0x10^22
4.0x10^22
2.0x10^22
8.0x10^20
6.0x10^20
4.0x10^20
2.0x10^20
0.0
Compacitance (1/F^2)
Reference
Dose = 1 x 10^14 cm^-2
Anneal at 300 °C
Anneal at 450 °C
-8
-7
-6
-5
-4
-3
-2
Voltage (V)

**Figure 11**

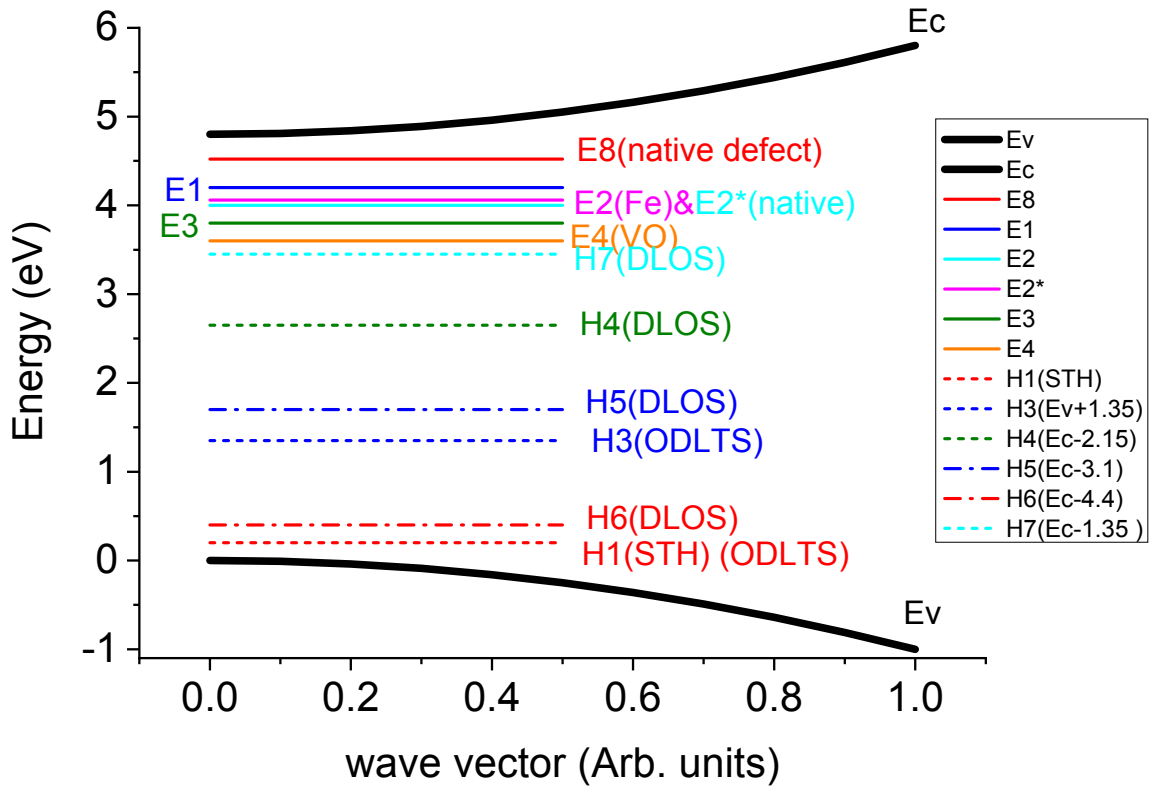
Ec
Ev
E8(native defect)
E1
E3
E2(Fe)&E2*(native)
E4(VO)
H7(DLOS)
H4(DLOS)
H5(DLOS)
H3(ODLTS)
H6(DLOS)
H1(STH) (ODLTS)
Energy (eV)
wave vector (Arb. units)
Ev
Ec
E8
E1
E2
E2*
E3
E4
H1(STH)
H3(Ev+1.35)
H4(Ec-2.15)
H5(Ec-3.1)
H6(Ec-4.4)
H7(Ec-1.35 )

**Figure 12**

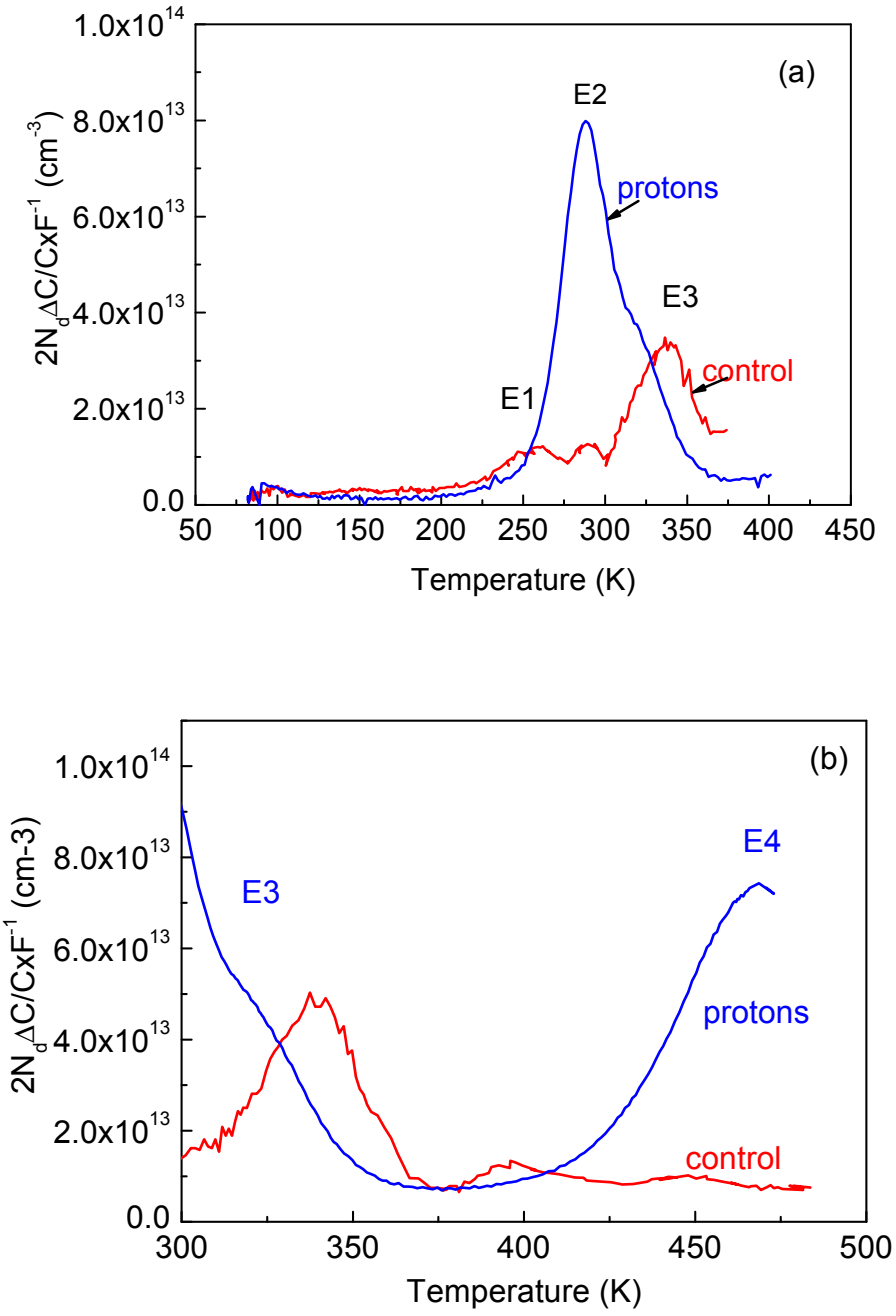
(a)
E1
E2
E3
protons
control
$2N_d\Delta C/CxF^{-1}$ ($cm^{-3}$)
Temperature (K)
(b)
E3
E4
protons
control
$2N_d\Delta C/CxF^{-1}$ (cm-3)
Temperature (K)

**Figure 13.**

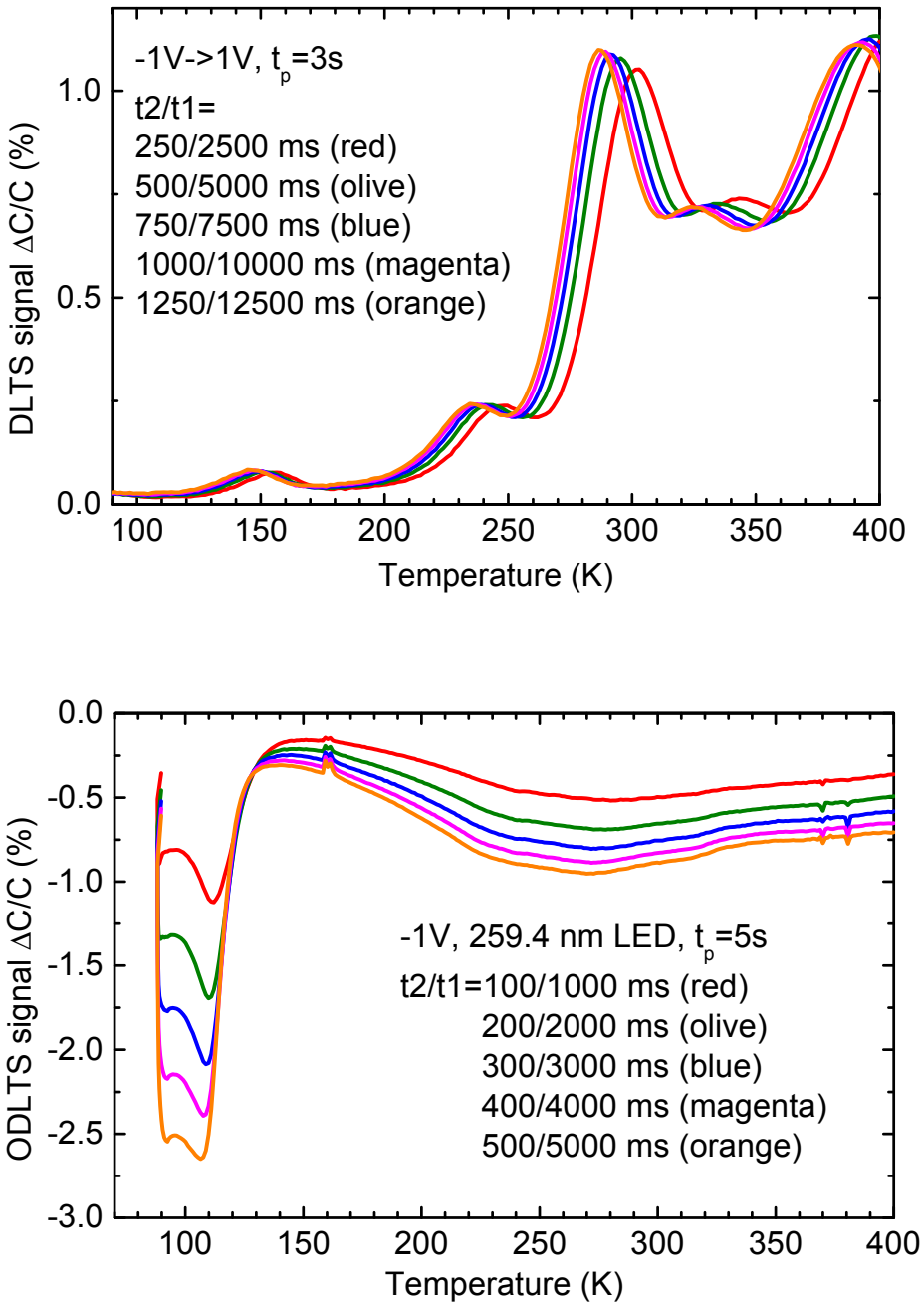
-1V->1V, t_p=3s
t2/t1=
250/2500 ms (red)
500/5000 ms (olive)
750/7500 ms (blue)
1000/10000 ms (magenta)
1250/12500 ms (orange)
DLTS signal ΔC/C (%)
Temperature (K)
-1V, 259.4 nm LED, t_p=5s
t2/t1=100/1000 ms (red)
200/2000 ms (olive)
300/3000 ms (blue)
400/4000 ms (magenta)
500/5000 ms (orange)
ODLTS signal ΔC/C (%)
Temperature (K)

**Figure 14**

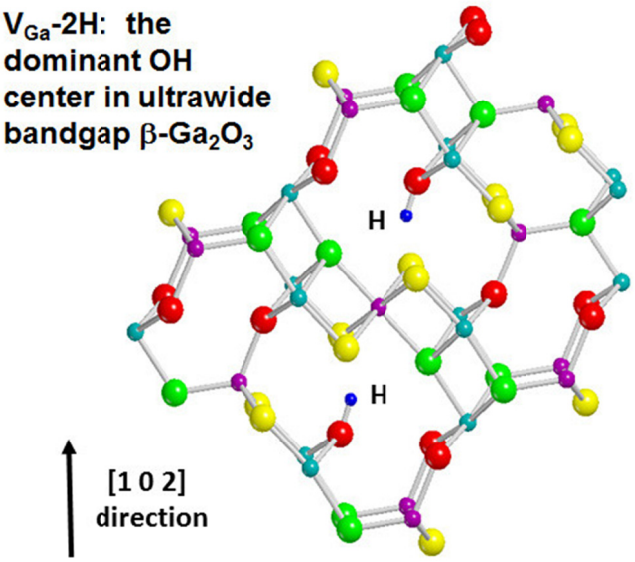
$V_{Ga}$-2H: the dominant OH center in ultrawide bandgap β-$Ga_2O_3$
H
H
[1 0 2] direction

**Figure 15**

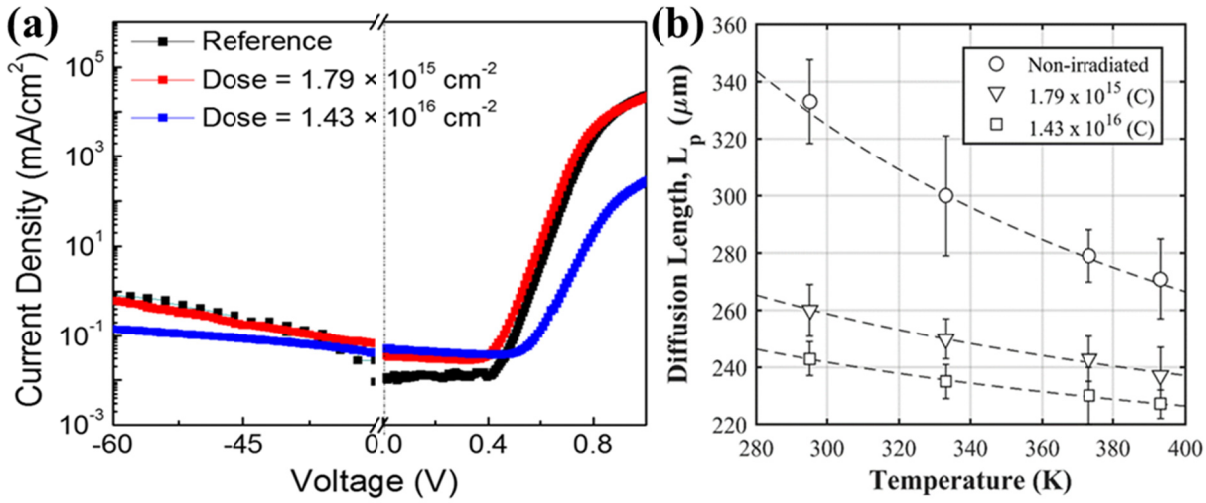
(a)
Reference
Dose = 1.79 × 10^15 cm^-2
Dose = 1.43 × 10^16 cm^-2
Current Density (mA/cm^2)
Voltage (V)
(b)
Non-irradiated
1.79 x 10^15 (C)
1.43 x 10^16 (C)
Diffusion Length, L_p (μm)
Temperature (K)

**Figure 16**

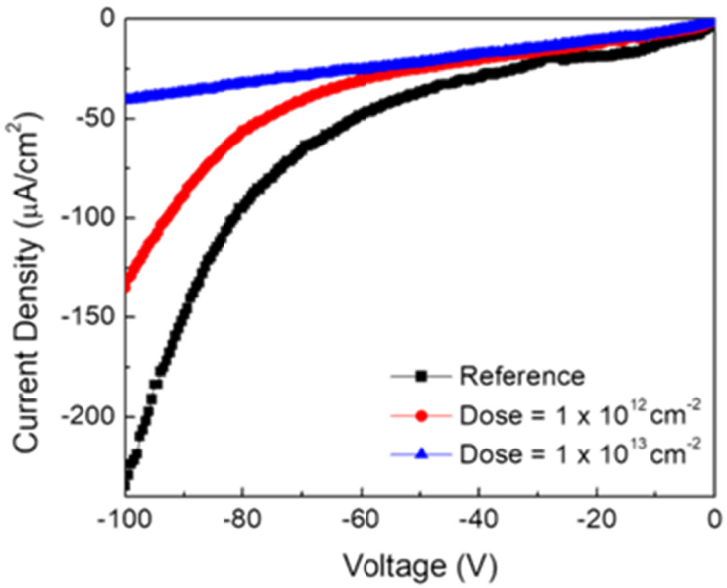


| | Reference | $10^{12}$ $cm^{-2}$ | $10^{13}$ $cm^{-2}$ |
|---|---|---|---|
| Barrier height (eV) | 1.09 | 1.05 | 1.04 |
| Ideality factor | 1.03 | 1.09 | 1.10 |
| $R_{ON}$ ($m\Omega.cm^{-2}$) | 4.0 | 22 | 62 |
| Drift region carrier concentration ($cm^{-3}$) | $8.3x10^{15}$ | $7.9x10^{15}$ | $1.03x10^{15}$ |
| Carrier removal rate($cm^{-1}$) | n/a | 406 | 728 |
| Reverse recovery time (ns) | 22 | 21 | 16 |
| On-off ratio (-1V) | $1.9x10^{7}$ | $7.5x10^{6}$ | $4.8x10^{6}$ |

**Figure 17**

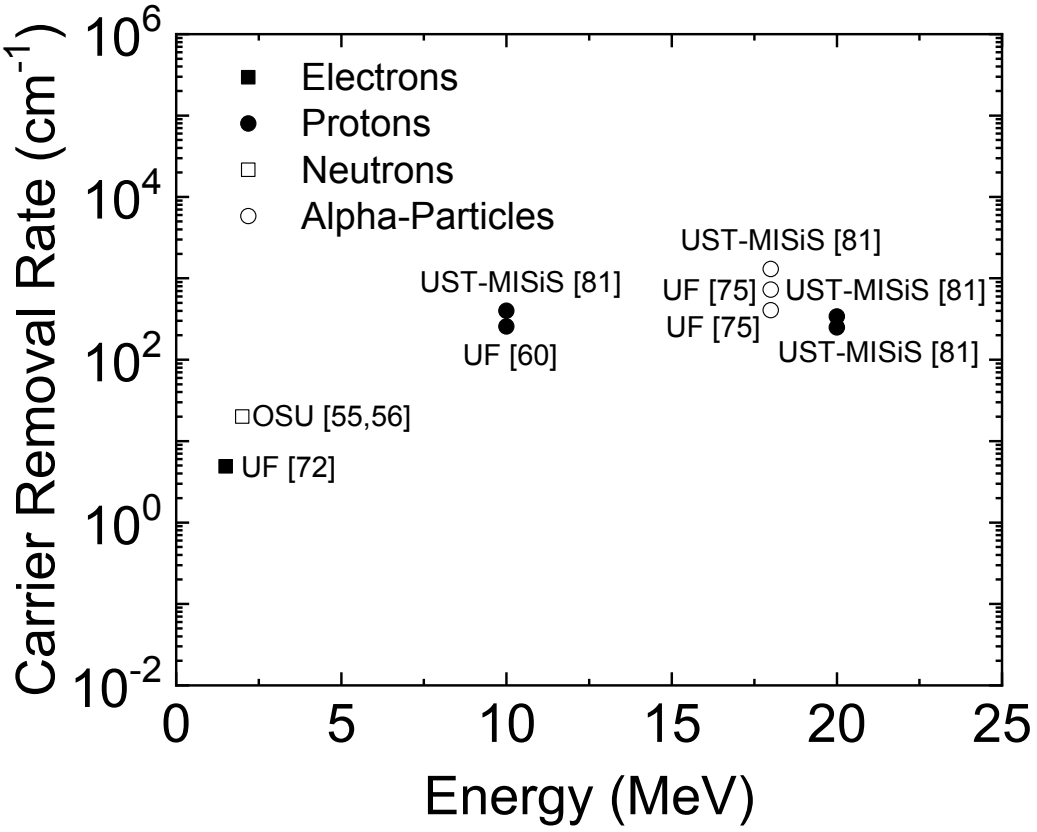
Carrier Removal Rate (cm-1)
Energy (MeV)
Electrons
Protons
Neutrons
Alpha-Particles
UST-MISiS [81]
UF [60]
UST-MISiS [81]
UF [75]
UF [75]
UST-MISiS [81]
UST-MISiS [81]
OSU [55,56]
UF [72]